Universidade de Aveiro Departamento de Química
2018

Tomás Coelho Almeida

Membranas poliméricas à base de fibroína para células de combustível

Silk fibroin-based polymeric membranes for fuel cells

Universidade de Aveiro Departamento de Química
2018

Tomás Coelho Almeida

Membranas poliméricas à base de fibroína para células de combustível

Silk fibroin-based polymeric membranes for fuel cells

Dissertação apresentada à Universidade de Aveiro para cumprimento dos requisitos necessários à obtenção do grau de Mestre em Engenharia Química, realizada sob orientação científica da Doutora Ana Margarida Madeira Viegas de Barros Timmons, Professora Auxiliar do Departamento de Química da Universidade de Aveiro e da Doutora Paula Cristina Vieira Barbosa, Investigadora Auxiliar do Departamento de Engenharia de Materiais e Cerâmica da Universidade de Aveiro.

Trabalho realizado com o apoio financeiro do projeto UniRCell POCI-01-0145-FEDER-016422 (Ref. SAICTPAC/0032/2015).

Dedico este trabalho aos meus pais.

o júri

Presidente: **Prof.ª Dr.ª Maria Inês Purcell de Portugal Branco**
Professora Auxiliar do Departamento de Química da Universidade de Aveiro

Prof. Dr. Fernando Manuel Bico Marques
Professor Catedrático do Departamento de Engenharia de Materiais e Cerâmica da Universidade de Aveiro

Dr.ª Paula Cristina Vieira Barbosa
Investigadora Auxiliar do Departamento de Engenharia de Materiais e Cerâmica da Universidade de Aveiro

agradecimentos

Deixo os meus agradecimentos à Professora Doutora Ana Barros e à Doutora Paula Barbosa, pela orientação científica e por estarem sempre disponíveis para a discussão de resultados e para me ajudarem no desenvolvimento deste trabalho.

Ao Doutor Filipe Figueiredo, pelo interesse demonstrado para com o meu trabalho e por todo o acompanhamento que lhe deu, sempre com vista à minha aprendizagem.

À Associação Portuguesa de Pais e Amigos do Cidadão Deficiente Mental de Castelo Branco, pela prontidão no fornecimento dos casulos do bicho da seda para serem utilizados neste trabalho.

Aos investigadores Eddy Domingues, Daniel Gil e Rambabu Gutru pela disponibilidade em fornecer ajuda e pela criação de um ambiente propício à aprendizagem.

Às investigadoras Sofia Bruno, Patrícia Neves e Margarida Antunes, também pela ajuda na criação de um ambiente propício à aprendizagem.

Aos meus colegas de curso, por terem estado do meu lado ao longo desta caminhada comum.

À direção de curso e aos professores com quem contactei, em particular ao professor Fernando Domingues, que leccionaram as suas unidades curriculares com o objectivo nobre de transmissão de conhecimento.

Aos meus pais e ao meu irmão, por todos os esforços que fizeram para que eu tivesse a possibilidade de estudar aquilo que queria, onde queria.

Por fim, agradeço à Rute, por ter estado sempre do meu lado, a partilhar experiências, emoções, e conhecimento, numa caminhada conjunta que sei que vai continuar.

palavras-chave célula de combustível, condutividade, membrana de electrólito polimérico, fibroína

resumo As pilhas de combustível de electrólito polimérico (PCEPs) têm sido amplamente estudadas devido à sua capacidade de produzir energia eléctrica de uma forma sustentável. No entanto, os materiais utilizados como electrólitos nas PCEPs apresentam impactos ambientais negativos. Assim, a procura de materiais alternativos é um aspeto crítico para melhorar a sustentabilidade deste tipo de tecnologias.

Esta dissertação visou o desenvolvimento de membranas poliméricas a partir de fibroína, uma proteína fabricada pelo bicho da seda, pouco explorada em aplicações relacionadas com células de combustível.

Numa fase inicial do trabalho foram testados dois métodos de extração e purificação da fibroina tendo-se selecionado aquele que se revelou mais reprodutível. Seguidamente estudou-se e otimizou-se as condições de preparação de membranas recorrendo a uma caracterização sistemática através de espectroscopia de infravermelho com transformada de Fourier (FTIR), difração de raios-X (XRD) e microscopia eletrónica de varrimento (SEM) tendo-se verificado que o processo de evaporação da água tem um impacto significativo na estrutura da fibroina. Com vista à aplicação em PCEPs, estudou-se ainda a capacidade de troca iónica (IEC), a adsorção dinâmica de vapor de água (DVS), assim como as propriedades térmicas e mecânicas. Os resultados obtidos confirmaram o efeito que o modo de preparação das membranas tem no seu desempenho, sendo de realçar os resultados de DVS. Estes resultados demonstram que nas membranas em que a conformação do tipo folhas-β é mais abundante, a adsorção de água chega a ser de 28% da sua massa, a 25 ℃. Por fim, avaliou-se a condutividade iónica recorrendo à espectroscopia de impedância variando a temperatura (T) e a humidade relativa (RH). As membranas de fibroína apresentam valores de condutividade de 5.7 $\times$ 10^{-7} S.cm^{-1}, a valores mais baixos de T e RH e de 1.8 $\times$ 10^{-3} S.cm^{-1} para T = 94℃ e RH = 98 %. Os valores obtidos são mais baixos quando comparados com membranas comerciais baseadas em Nafion®, no entanto, as membranas de fibroína apresentam resultados promissores no que diz respeito a propriedades térmicas e mecânicas, com temperaturas de degradação superiores a 260 ℃. Sendo um biopolímero com propriedades de base promissoras, a fibroína apresenta-se assim como um material com potencial aplicação em PCEPs.

keywords fuel cell, conductivity, polymer electrolyte membrane, silk fibroin

abstract Polymer electrolyte fuel cells (PEFCs) have been widely used for their ability to generate electricity in a sustainable way. However, the materials used in PEFCs present themselves with clear negative environmental impacts. Thus, the search for alternative materials is a critical aspect in order to improve the sustainability of such technologies.

This dissertation aimed at the development of polymeric membranes of silk fibroin, a protein produced by the domestic silkworm, not thoroughly explored for fuel cell related applications.

In an initial phase of this work, two methods for fibroin extraction and purification were tested and the one that proved to be more reproductive was chosen. After that, the membrane preparation conditions were studied and optimized, using Fourier transform infrared spectroscopy (FTIR), X-ray diffraction (XRD) and scanning electron microscopy (SEM), and a significant impact on the structure of fibroin by the evaporation process of water was verified. Considering the application in PEFCs, the ion-exchange capacity (IEC), dynamic water vapor sorption (DVS), thermal and mechanical properties were also studied. The obtained results demonstrated that when the β-sheet fraction is higher in the membrane structure, water sorption is up to 28% of its mass, at 25 ºC. Finally, the ionic conductivity of the membranes was evaluated by impedance spectroscopy, at different temperature (T) and relative humidity (RH) conditions. Silk fibroin membranes present ionic conductivity values ranging from 5.7 $\times$ 10^{-7} S.cm^{-1}, at lower temperatures and relative humidities, to 1.8 $\times$ 10^{-3} S.cm^{-1} at RH = 98% and T = 94ºC. The obtained values for conductivity are lower when compared with commercial membranes based on Nafion®, however, the silk fibroin membranes still demonstrate promising results regarding thermal and mechanical properties, with degradation temperatures up to 260 ºC. As a biopolymer with such promising properties, silk fibroin is a material with potential application in PEFCs.

Contents

List of Figures

List of Tables

Abbreviations and chemical formulas

AA	Adipic acid
AC	Alternate current
Ala	Alanine
AMPS	2-Acrylamido-2-methylpropane sulfonic acid
ATR	Attenuated total reflectance
BC	Bacterial cellulose
C_2H_6O	Ethanol
$CaCl_2$	Calcium chloride
CO_2	Carbon dioxide
Cu	Copper
DMA	Dynamic mechanical analysis
DVS	Dynamic vapor sorption
EDS	Energy dispersive x-ray spectroscopy
IS	Impedance spectroscopy
FCV	Fuel cell vehicle
FTIR	Fourier transform infrared spectroscopy
GDL	Gas diffusion layer
Gly	Glycine
GPC	Gel permeation chromatography
H^+	Proton
H_2	Hydrogen
H_2O	Water
H_2SO_4	Sulfuric acid
H_3PO_4	Phosphoric acid
HCl	Hydrochloric acid

IEC	Ion exchange capacity
IP	In-plane
IR	Infrared
K_2SO_4	Potassium sulfate
KOH	Potassium hydroxide
LCR	inductance (L_i) capacitance (C) and resistance (R)
LiBr	Lithium bromide
MEA	Membrane electrode assembly
Mg	Magnesium
MWCO	Molecular weight cut-off
Na_2CO_3	Sodium carbonate
NaCl	Sodium chloride
NaOH	Sodium hydroxide
NH_4Cl	Ammonium chloride
O^{2-}	Oxide ion
O_2	Oxygen
OH^-	Hydroxide ion
ORR	Oxygen reduction reaction
PDI	Polydispersity index
PEFC	Polymer electrolyte fuel cell
pH	Potential of hydrogen
PLA	Poly(lactic acid)
Pt	Platinum
PVA	Poly(vinyl alcohol)
RH	Relative humidity
SAC	Silk-derived activated carbon
SEM	Scanning electron microscopy
Ser	Serine
SF	Silk fibroin
SS	Silk sericin
TFE	Tetrafluoroethylene
TGA	Thermogravimetric analysis

Thr	Threonine
TP	Through-plane
Tyr	Tyrosine
UTS	Ultimate tensile strength
UV	Ultraviolet
V	Volt
Val	Valine
XRD	X-ray diffraction
$-SO_3H$	Sulfonic group

Symbols

A	Area	m^2
Conc	Concentration	$mol.dm^{-3}$
C	Capacitance	Farad
D	Distance	m
d	Interplanar distance	Å
E	Young's Modulus	Pa
F	Force	N
f	Frequency	Hz
h	Thickness	µm
He_r	Heating rate	$°C.min^{-1}$
I	Electrical current	A
J	Current density	$A.m^{-2}$
L	Length	m
L_i	Inductance	H
M_w	Average molecular weight	$g.mol^{-1}$
P	Pressure	Pa
R	Electrical resistance	Ω
R_g	Ideal gas constant	$J.K^{-1}.mol^{-1}$
S	Surface area	m^2
Sc	Specific capacity	$mAh.cm^{-2}$
T	Temperature	K,°C
t	Time	s
Ts	Tensile strength	MPa
V	Voltage	V

V_0	Maximum voltage	V
Vol	Volume	cm^3
W	Weight	g
W_d	Width	m
Z	Electrical impedance	Ω
Z'	Electrical impedance (Real component)	Ω
Z"	Electrical impedance (Imaginary component)	Ω
δ	Phase angle (Impedance and Dynamic Mechanical Analysis)	°
θ	Diffraction angle	°
λ	Wavelength	Å
σ	Electrical conductivity	$S.cm^{-1}$
ω	Angular frequency	$rad.s^{-1}$

1. Preamble

In a time of growing worries on the diminishment of fossil fuels and their global increasing demand, sustainability and environmental impact have become two of the greatest factors influencing the development of new methods for energy production, in an attempt to deal with the shortage of resources as well as reducing the harmful impacts of fossil fuels in nature.

Fuel cells have been widely studied for their ability to produce energy continuously (as long as fuel is continuously provided), in a truly sustainable paradigm. However, there are still some disadvantages when it comes to long term reliability, operations in high temperature/low humidity conditions, and the need to use expensive catalysts. Development of new technologies in this field is also still conditioned by the low availability of high ionic conductivity electrolytes that surpass Nafion®, developed by DuPont in the 60s. The objective of this work is to address some of those disadvantages, in an attempt to change the current status of fuel cell technology. In this sense, this work intends to develop bio-polymeric membranes based on silk fibroin (SF), to serve as an environment-friendly electrolyte for polymer electrolyte fuel cells and other related applications such as electrolyzers, electrochromic devices or batteries.

This dissertation is divided into 5 Chapters. After this preamble, Chapter 2 deals with the principles of fuel cell technology and outline the material's requirements for advanced alternative polymer electrolyte fuel cells. In Chapter 3, the materials and methods used in this work are described. The results obtained are presented and discussed in Chapter 4. Finally, Chapter 5 aims to provide directions and suggestions that might be interesting for the development of next-generation materials.

2. Introduction

In this section, a small revision of the state of the art is presented, with the purpose of putting the developed work in perspective. Therefore, this chapter begins with a general approach to fuel cell technology, and then follows with the state of the art on polymer electrolytes for polymer electrolyte fuel cells.

2.1. Polymer Electrolyte Fuel Cells (PEFCs)

Fuel cell technology has been widely promoted as a field of research, and has shown promise on the development of alternative ways to produce energy.

Fuel cells are electrochemical devices that convert free energy from a chemical reaction to electrical energy, providing high efficient power generation and low environmental impact, since combustion is avoided. [1] The conversion continues uninterrupted as long as fuel and oxidant are supplied, which is the main difference in relation with batteries, since these have a limited shelf-life. [2] This means fuel cells are actually "factories", continuously transforming chemical energy from a fuel into electricity. [3]

Figure 1 is a representation of a PEFC, also referred as the solid polymer fuel cell. The generally used electrolyte on PEFCs is an ion exchange membrane (a fluorinated sulfonic acid polymer, trade name Nafion®, or similar) that works as a proton conductor.

The components of a single fuel cell of this type include an electron conducting anode (a porous layer to allow gas diffusion and an anodic catalyst layer), a proton conducting electrolyte, which must be hydrated, an electron conducting cathode (a cathodic catalyst layer and a porous gas diffusion layer - GDL), and current collectors. The latter are bipolar plates in a stack, which comprise about 90% of the total fuel cell volume, and are the most expensive component of the fuel cell. The assemblies of the anode, electrolyte,

and cathode are commonly referred as the Membrane Electrode Assemblies (MEAs), "the heart of the fuel cell". [2]

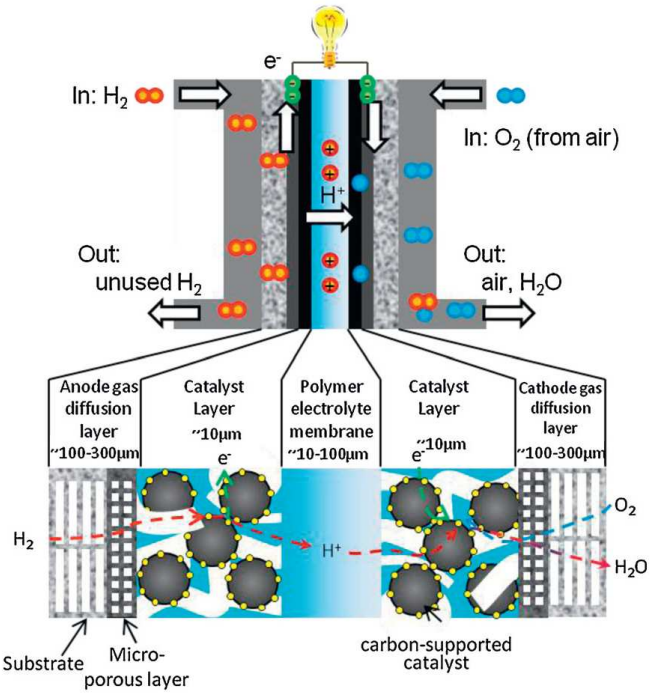

Figure 1 – Schematic of a PEFC. [4]

The electrochemical reactions take place at the electrodes, and produce electrical current continuously, while the electrolyte conducts ionic species. Two reactions take place: the fuel oxidation in the anode side and the oxidant's reduction in the cathode side. The global chemical reaction that takes place when pure hydrogen and oxygen are used (reducing agent and oxidant, respectively), is described in scheme 2.1. The electrochemical reaction produces energy in the form of heat.

$$\mathrm{H_2} + \frac{1}{2}\,\mathrm{O_2} \longrightarrow \mathrm{H_2O} + \mathrm{Energy} \tag{2.1}$$

The electrolyte is one of the most important constituents of this type of fuel cell. Besides the requirement of high ionic conductivity (between 0.01 and 0.1 $\mathrm{S.cm^{-1}}$), it must also have good mechanical properties, in both dry and hydrated states, chemical stability in acidic and alkaline environments and good thermal properties. The electrolyte should also present low physical permeability to liquids and gases, to allow diffusion of the fuel due to the electrochemical gradient. The material used should also be relatively low-cost, sufficiently durable, and of easy fabrication. PEFCs can operate in a range

of temperatures that goes from the average room temperature of 25 °C up to 220 °C, which will also require thermal stability of the materials used as electrolytes at these temperatures. [1–3]

PEFCs have been widely pursued for a variety of applications, such as fuel cell vehicles (FCV) and other portable applications, due to various reasons. For once, the usage of a solid electrolyte provides excellent resistance to fuel permeability. The lower operating temperatures of PEFCs are also attractive, because it reduces start-up time and corrosion. Current densities of over 2 $kW.L^{-1}$, higher than other fuel cell types, are also one of the most important reasons why PEFCs continue to be the most researched type of fuel cells. [1]

The voltage generated by an individual fuel cell however, is of about 0.6-0.7 V instead of the theoretical 1.2 V, due to ohmic losses, which is too low for practical applications. [5] Thus, it is necessary to stack multiple cells in series, as represented in Figure 2, and cell stacks connected in parallel, to achieve the desired voltage for each application. Because the polymeric membrane must be always hydrated to allow proton conduction (but not flooded), water management is critical for maintaining the normal functioning of the system and has to be performed by a cooling system, despite the narrow operating temperatures of PEFCs.

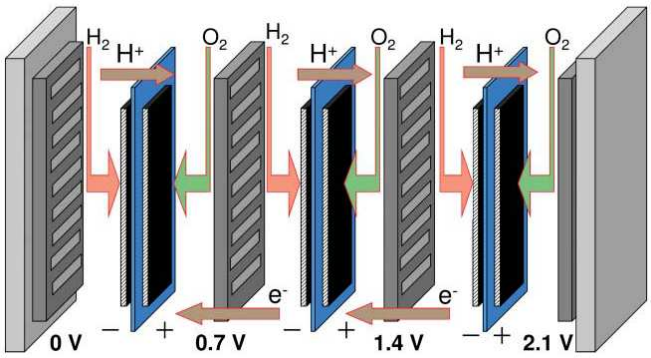

Figure 2 – Simplified representation of a fuel cell stack (in series). [5] The system's voltage is the sum of all of the individual cell's voltages.

PEFCs also require the usage of high loads of platinum as a catalyst in both the cathode and anode, which is one of the major setbacks of this fuel cell type. The anode is easily poisoned by small amounts of carbon monoxide, sulfur or halogens, and the bypass options can be fuel pre-treatment, or increasing the platinum load. Both options will have a negative impact on the operating costs, system complexity, and overall efficiency.

2.2. Polymer electrolytes

The prerequisites for fuel cell electrolytes have been a big set back for the development of novel materials for this application. The polymeric material used must have three main roles: charge carrier, reactant gases separator and electronic insulator (to prevent electron diffusion through the membrane).

The most commercially used membranes in PEFC are based in an acid-functionalized perfluorinated copolymer developed by DuPont in the mid 60's, [6] later designated as Nafion®. The poly(perfluorosulfonic acid) structure of Nafion® consists of hydrophobic tetrafluoroethylene (TFE) backbones and pendant side chains with hydrophilic terminated sulfonic groups which are responsible for high proton conductivities when fully hydrated. The chemical structure of Nafion® is represented in Figure 3. [7]

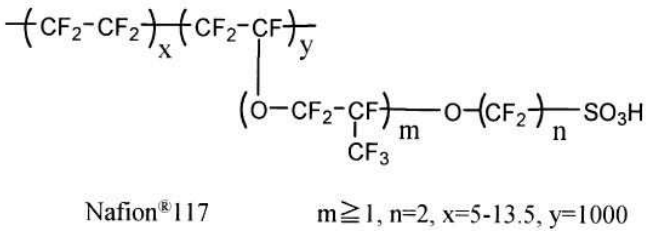

Figure 3 – Chemical structure of Nafion®. [7]

Due to the balance between the hydrophilic and hydrophobic parts of the chemical structure, Nafion® ends up with a decent water uptake, and values of proton conductivity up to 10^{-1} S.cm^{-1} in satured conditions. [8] This value, however, decreases dramatically at working temperatures above water's boiling point, which causes the membrane to lose its water content. [7]

The proton conducting mechanism of Nafion® can be of different types, depending on the level of membrane hydration. The most important ones are the "proton hopping mechanism", also named as "Grotthus mechanism" or "structural diffusion mechanism", and a second mechanism considered as "vehicular".

In the Grotthus mechanism, represented in Figure 4. [9] protons "hop" from one water molecule to another across the membrane. The proton produced by hydrogen in the anode side of the fuel cell connects with a water molecule and, with the help of the rotation of water molecules, will be transported across the membrane. When the water content is decreased, the sulfonic groups (SO_3^-) in the structure of Nafion® assist this

mechanism by allowing the proton to reach the water molecules that will be no longer closer enough to carry the mechanism on their own. The same process continues with the following sulfonic groups and water molecules until the proton reaches the other side of the membrane. This proton conduction mechanism normally occurs for low humidity levels and has a small contribution to the conductivity of Nafion®. [10]

The "vehicular mechanism" is another important mechanism that involves water working as a vehicle. The proton produced in the anode side connects with a water molecule and forms an hydronium ion, which will diffuse through the aqueous medium until it reaches the other side of the membrane, as described in Figure 4 by the blue line. [9]

For this mechanism to occur, free volume within the polymer chains must be reasonable, to allow the hydrated protons to be transferred throughout the membrane. The hydrophobic backbone of Nafion® makes water transfer easier because of the repelling interactions between water molecules and the surface. [11] The vehicular mechanism is more significant than the Grotthus mechanism and depends on the membrane's degree of hydration.

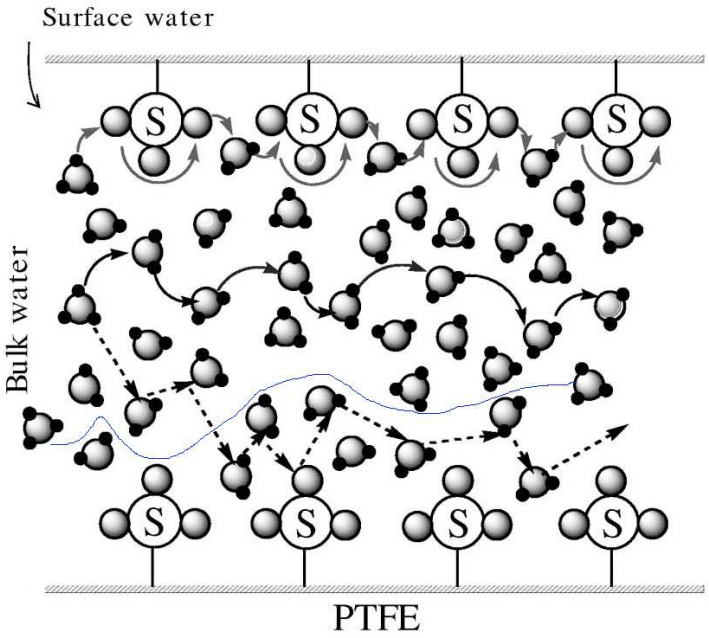

Figure 4 – Simplified scheme of the proton transport mechanisms in Nafion. [9]

Nafion® membranes work excellently at low and medium temperatures (up to 80-100 °C),

when fully hydrated, and have good mechanical and thermal stability. [12] On the other hand, this type of fluorinated membranes allow fuel permeability and have lower values for conductivity at high temperatures (above 100 °C) and/or low relative humidities (which reduces the membrane hydration level). Also, and since the fluorine chemistry implies a great deal of investment, the production of Nafion® membranes is expensive. [7, 12]

Alternatives for surpassing the limitations of Nafion® have been developed, such as mixing with other materials including fillers, copolymerization, and development of new materials as substitutes. [13] The latter are usually categorized as perfluorinated (or partially fluorinated), non-fluorinated, and acid-base blends. Although some of the membrane materials presented in Figure 5 [11, 13] surpass some of the difficulties of Nafion®, they also present some disadvantages, from lower proton conductivity to lower durability, which might be some of the reasons why Nafion® continues to be the membrane electrolyte of choice in PEFC's. Some of the materials in Figure 5 have their names reported in Section A.1.

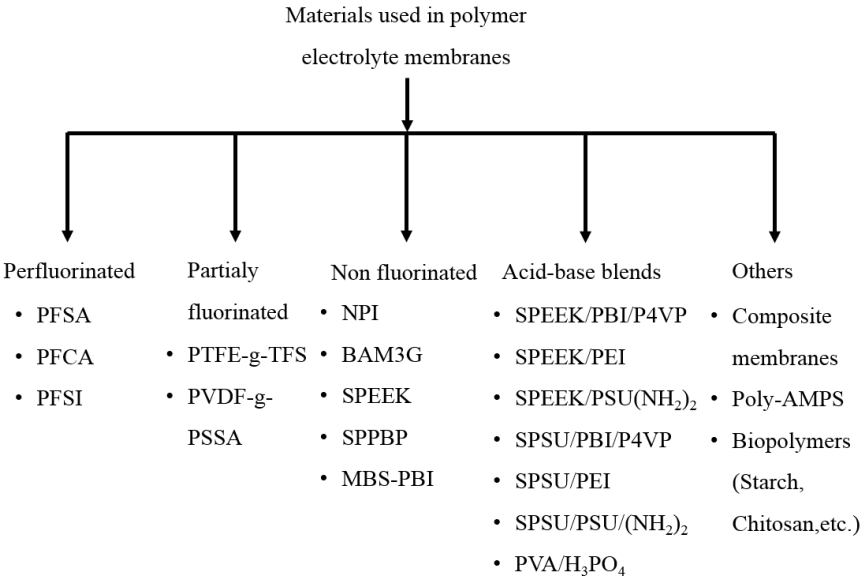

Figure 5 – Classification of membrane materials. [11, 13]

Research on environmental friendly materials to serve as electrolytes has been increasing lately. Biomaterials such as chitosan, starch, bacterial cellulose, silk fibroin, and others require a low use of chemicals to get processed into membranes/films, and are generally very abundant, making these materials potential candidates for application in fuel cell technology in a more eco-friendly way.

Chitosan has been extensively studied lately for application as a membrane electrolyte or electrode in many types of PEFCs, such as alkaline fuel cells (AFCs), proton exchange membrane fuel cells (PEMFCs) and direct methano fuel cells (DMFCs). Being a naturally abundant material, it has the advantage of lowering the overall fuel cell cost significantly. [14] Chitosan blends with other materials have been thoroughly studied, such as the ones with poly(vinyl alcohol) (PVA), or the ones combining chitosan with a blend composed of a commercially available copolymer, 2-Acrylamido-2-methylpropane sulfonic acid (AMPS) and acrylic acid (AA) which gives values for conductivity of 3.59×10^{-3} S.cm^{-1} at 30 °C, [14] and provides more tolerance to fluctuations in water content, ensuring higher ionic conductivity than Nafion® at higher temperatures and/or lower humidities. [15] Both the Grotthus and vehicular mechanism are thought to play an important part in the ionic conductivity of such blends. [14] A scheme representing the proton conduction mechanisms present in chitosan-P(AA-AMPS) blends is presented in Figure A.1.

Starch (or amylum) has also been investigated, and has been incorporated in blends with other materials, such as chitosan and ammonium chloride (NH_4Cl). Conductivity for membranes prepared by solution casting of these blends reaches values of 5.11×10^{-4} S.cm^{-1} with the addition of 35 wt% of glycerol. [16] Starch has also been studied for implementation in enzymatic fuel cells (which use biocatalysts instead of platinum), [17] and showed good results when it comes to hydrogen production yields. [18] However, starch has not been studied for fuel cell related applications as a single material.

Bacterial cellulose (BC) is an organic compound generated by bacteria such as *Acetobacter*, and has also been studied for application in PEFCs, because of its good thermal stability and mechanical properties. BC is formed by nanofibrils, and has improved properties in relation to plant cellulose, such as higher crystallinity, higher water uptake, and higher tensile strength. BC/PSSA composite membranes can provide values for proton conductivity of up to 0.1 S.cm^{-1}. [19]

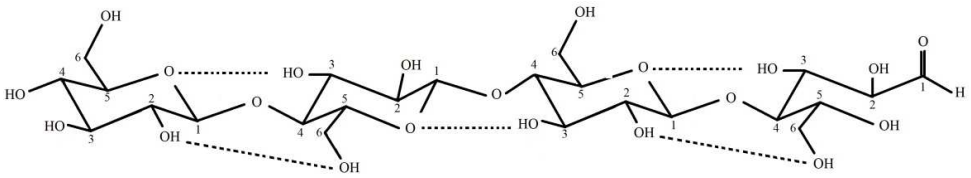

Figure 6 – Chemical structure of bacterial cellulose, with intra molecular hydrogen bonding. [20]

2.3. Silk

Silk is a product of the so called sericulture, the art of raising silkworms for the production of cocoons, such as the ones shown on Figure 7b, which in turn are the raw material for silk weaving. As the only known natural fiber which organizes itself as a continuous, strong thread, silk has been extensively used as a luxury material for textile fabrication for a long time, [21] being one of the oldest fibers known to man. [22]

Many insects produce filaments than can be used for silk production, but only the one produced by the mulberry silk moth *Bombyx mori* (Figure 7a) and a few others in the same family are used by the silk industry[1]. [22]

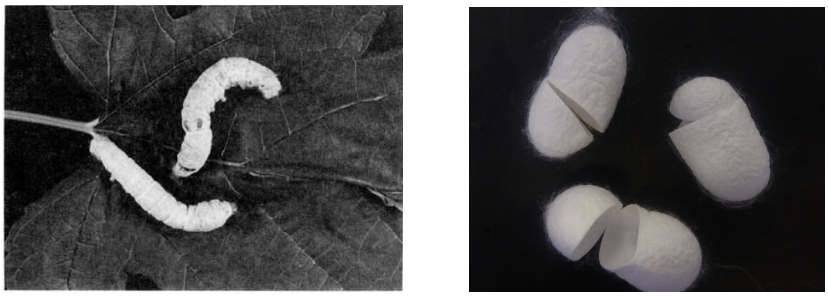

(a) (b)

Figure 7 – (a) *Bombyx mori* species [24] and (b) *Bombyx mori* silkworm cocoons, used in silk production.

Other insects, mainly spiders, of the species *Araneus diadematus* and *Nephila clavipes*, produce spidroin, the spider version for fibroin, which has a different crystalline structure and is used in a small number of applications, such as weapon cross-hairs and other optical instruments. [25]

Normally, silkworms breed once a year. However, under controlled temperature and humidity conditions, eggs from *Bombyx mori* species can be hatched three times per year, with around 350-400 eggs per specimen. [22] Each egg can result in 1000 to 1500 meters of silk thread, which in turn allows the constant supply of silk fibers to the industries that require it.

2.3.1. Composition and structure

Fibroin and sericin, which can be seen in Figure 8, are two high molecular weight proteins and are considered to be the main constituents of silk (with 65-75% of silk being attributed to fibroin, 20-30% to sericin, and the remaining 5% to wax, sugars and

[1] The best raw silk is obtained from *Bombyx mori* species from India, which have mutated throughout time to end up having much more tolerance to high temperature and humidity conditions. [23]

other impurities). [26] The first is used in silk production, due to its structural strength, while the second works like an adhesive, joining the fibroin filaments together (which gave it the "silk glue" designation). [22]

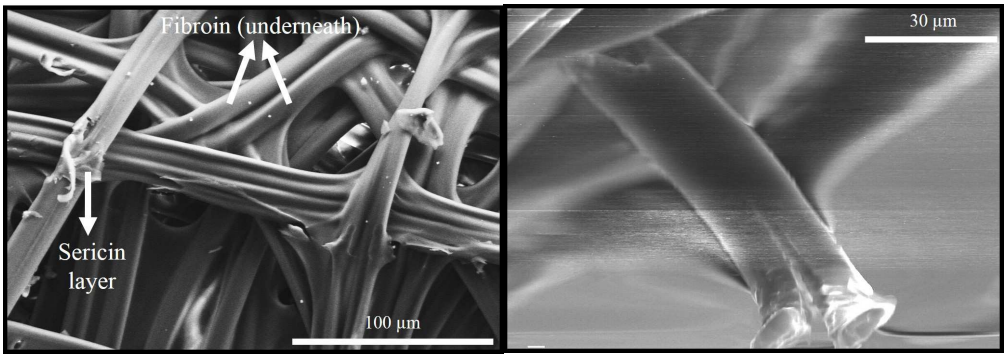

(a) (b)

Figure 8 – (a) SEM image of a *Bombyx mori* cocoon and (b) Image of two threads of fibroin. It can be seen that they are enveloped with an external layer of the silk glue, sericin. [22]

Sericin is a highly hydrophilic molecule with a molecular weight that ranges from 20 000 to 40 000 Da ($g.mol^{-1}$), consisting on 18 amino acids, with a high content of serine (about 33%), an amino acid that makes sericin water-soluble. Sericin's polar groups, solubility, and structural organization enable crosslinking and combinations with other polymers, providing unique properties, such as antioxidant, moisturizing, healing and antibacterial, which in turn allows it to be used in a variety of applications, mostly in cosmetics and medicine. [27,28]

The molecular structure of sericin is not yet well defined, but a model has been proposed, which is presented in Figure 9. [29] The secondary and tertiary structures have also been studied, with proposed models, such as the one presented in Figure 10, [30] in which it can be observed the existence of both random coils and β-sheets in sericin's tertiary structure. The glue-like property of sericin is attributed to hydrogen bonding between serine residues of sericin with serine residues of fibroin, which has a serine percentage of 12% [31]

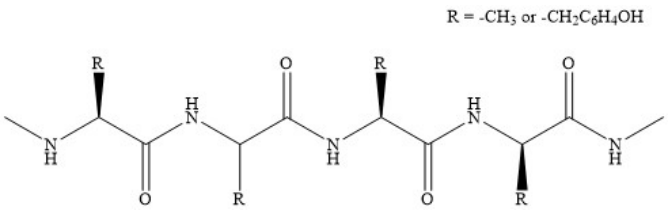

Figure 9 – Silk sericin proposed primary strucure. [29]

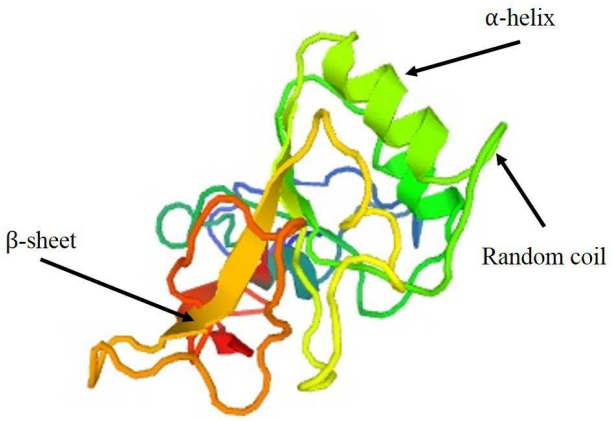

Figure 10 – Silk sericin proposed tertiary strucure. [30]

Silk fibroin (SF) is a large molecular weight protein (200-350 kDa or more) with repeating hydrophobic domains interrupted by small hydrophilic groups. [32] These domains, when linked, generate high molecular weight chains, with characteristic N and C termini. [21]

Fibroin from the *Bombyx mori* silkworm consists of a heavy chain (H-fibroin), a light chain (L-fibroin) and a smaller polypeptide named "P25" (25 kDa). The first two are linked by a disulfide bond at their C-terminus, while "P25" is non-covalently linked to the other chains in the terciary structure of fibroin. [33]

The L-fibroin chain is hydrophilic and contains Ser, Ala, Gly, and a N-acetylated Ser residue. [21] H-fibroin is mainly composed by non-polar and hydrophobic groups such as Glycine (Gly, 45%), Alanine (Ala, 26%), Tyrosine (Tyr, 5%) and the hydrophilic Serine (Ser, 12%). [32] Many studies have suggested a primary structure for fibroin, but it is only known that about 70% of *Bombyx mori* fibroin consists on the amino acid sequence (-Gly-Ser-Gly-Ala-Gly-Ala-)n, represented in Figure 11. [33,34]

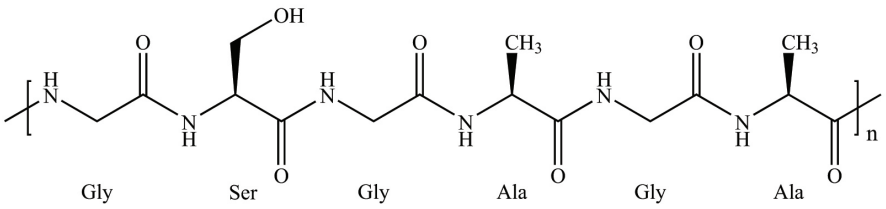

Figure 11 – Amino acid sequence of H-fibroin, [35] which is about 70% of the structure of SF.

It also has been known for a while that the H-fibroin chain is formed by a highly repetitively crystalline fraction of Glycine-X units, in which X can be Ala, Ser, Val, Tyr

or Threonine (Thr). [35] The proposed composition of H-fibroin is presented in Table A.2.

Silk fibroin co-exists in three forms, which have been named as Silk I, II and III. Silk III is only present in the liquid-vapor interface, and therefore has not been explored since discovery. Silk I is a less crystalline structure formed inside the silkworm glands, before being used for cocoon spinning purposes, consisting on α-helice. After spinning, SF has the ability to self-assembly, and creates large crystalline regions, forming a new, stronger structure (Silk II). [21,32]

The secondary, crystalline structure of SF (Silk II) is mainly composed by anti-parallel β-sheets (as shown in Figure 12), [34] formed by hydrogen bonding between amide linkages of adjacent chains and hydrophobic interactions. [36] These β-sheets[2] are highly ordered and have small bond lengths (around 2.7Å), which give silk outstanding tensile strength.

The less ordered part of the secondary structure has a small number of less ordered structures, such as α-helices (Silk I) and random coils. The latter are amorphous. [36]

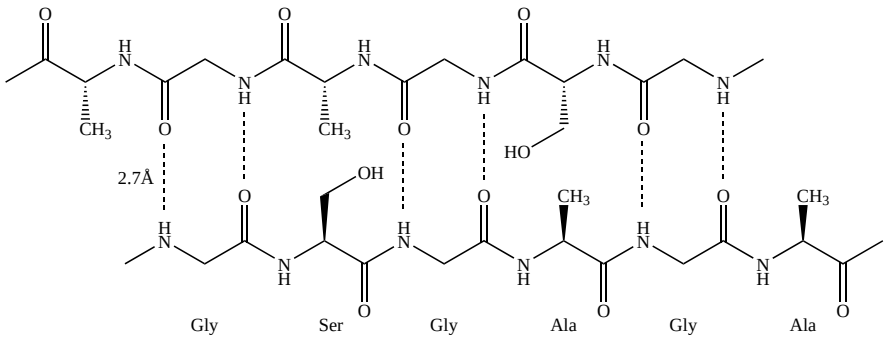

Figure 12 – General schematic of the anti-parallel β-sheets present in *Bombyx mori* SF. Anti-parallel β-sheets possess a shorter bond length between atoms than simple parallel sheets (2.7Å $<$ 2.97Å), and therefore are stronger. [36]

The self-assembly mechanism of SF consists on the formation of micellar-type structures, with large hydrophilic blocks in the outer edges, while the large hydrophobic blocks and small hydrophilic blocks are inside the micelles, with a random distribution. [38] If the structure undergoes crystallization, the hydrophobic blocks inside the micelles arrange gradually into β-sheets by hydrogen bonding and hydrophobic interactions, whilst the small hydrophilic blocks move to the surface of the micelles to interact with water. Figure 13 is a visual representation of the self-assembly mechanism that SF undergoes. [38]

[2]The prefix (β) is due to the fact that these structures were the second proposed William Astbury, after the α-helices, in the early 1930s. The structures were later refined by Linus Pauling and Robert Corey, in 1951. [37]

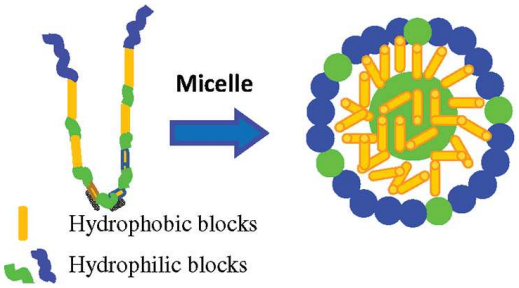

Figure 13 – Self-assembly model of SF [38].

The separation of fibroin from sericin consists on boiling the *Bombyx mori* silkworm cocoons, in which sericin, being a hydrophilic molecule, will be transferred into the aqueous solution. SF, however, behaves as a greatly hydrophobic molecule, and will remain suspended as an agglomerate of fibers. This procedure, illustrated in Figure 14, is commonly called degumming, since it consists on the removal of a "gum" or "glue", in this case, sericin.

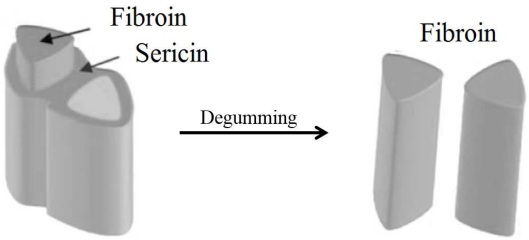

Figure 14 – Basic illustration of the degumming procedure. [36]

Degumming can be performed in boiling water, as it was done by the Ancient Chinese, but it takes many hours to reach maximum efficiency, and extensive degumming times can start to degrade fibroin. Degumming time can be reduced by turning the solution acid ($pH \leq 2.5$) or basic ($pH \geq 9$), which can be performed by using a variety of solvents, namely high concentrated urea, Marseille soap (made from vegetable oils), or sodium carbonate (Na_2CO_3). [26] Enzymatic degumming can also be performed, but its efficiency is not suitable for concrete applications. The most common degumming method consists on boiling the silkworm cocoons in 0.5% Na_2CO_3 for 30 minutes, for maximum degumming degree and lower fibroin degradation. [26]

After degumming, the fibroin fibers can be dissolved with the help of a swelling agent, such as lithium bromide (LiBr) or a ternary solvent system consisting on water, calcium chloride and ethanol (H_2O:$CaCl_2$:C_2H_6O), for example. The resulting solution (after removing the swelling agent) is commonly referred as regenerated silk fibroin (RSF). [39]

Some properties of native fibroin, namely mechanical, will be affected by this processing. However, dissolution is important if the application requires fibroin to be in a liquid form. [39]

2.3.2. Properties and applications of silk fibroin

SF benefits from being a low-cost and abundant material, as each insect yields a great amout of fibroin. The most useful properties of silk fibroin have always been considered to be its mechanical properties. SF derived from the *Bombyx mori* species has a high value for its ultimate tensile strength (between 300 and 740MPa), [36] and also possesses higher toughness than of some synthetic fibers, such as Kevlar®. These results are a consequence of the structures formed by SF, referenced in the prior Section. [32] Table 1 shows values of some mechanical parameters, in comparison with other materials. [36,40]

Table 1 – Mechanical data of SF along with other materials (adapted). [36, 40]

Material	Young's Modulus (GPa)	Ultimate strength (MPa)	Toughness ($MJ.m^{-3}$)
Bombyx mori SF	10-17	300-740	70-78
Spider silk (*Nephila clavipes*)	10.9	875	–
Nylon	1.8-5	430-950	80
Kevlar	130	3600	50
Polylactic acid (PLA)	1.2-3.0	28-50	–

In terms of thermal properties, the glass transition of SF occurs at around 178 °C. SF also exhibits an endothermic peak at around 100 °C which is attributed to the loss of bound water. Degradation starts at around 280 °C. All of these values have been obtained by multiple studies on the SF fibers, [41–43] and changes in the crystallinity of SF are also known to influence the glass transition and degradation temperatures. [44,45]

Two of the most important features of SF are its biocompatibility and biodegradability. Its surface chemistry allows controllable and easy degradation, making SF a promising biomaterial, being already explored in various medical fields, such as tissue engineering and drug delivery. [21,36]

In the fuel cell field, and since the catalyst used in both the cathode and anode side is of high cost (Platinum), SF has been studied for incorporation in the PEFC's cathode, in the form of silk-derived activated carbon (SAC), due to the existence of nitrogen atoms within the structure of SF, which have been known to play a role in the oxygen-reduction

reaction (ORR). [46] The results of this study suggested that silk fibroin could work as an "active support" in the cathode's catalyst.. [46]

Jia et. al fabricated a thin-film Mg battery with an electrolyte composed of SF and an ionic liquid. [47] The battery showed values for specific capacity of 0.06 $mAh.cm^{-2}$. More recently, SF has been investigated has an electrolyte for electrochromic devices, because of its very high transparency when processed into films, and showed promising results in terms of switching speed and coloration efficiency. [48]

Employment of SF as an environmental friendly separator for lithium ion batteries has also been studied, proving that SF rich in β-sheet conformations has excellent cycling performance and conductivity values higher than 0.1 $mS.cm^{-1}$, which is the minimum value required for lithium ion battery separators. [49] These results are directly associated with a more planar structure of SF's crystalline fraction, which establishes interactions with the lithium ions, [49]

In this work, SF will be considered as a possible polymeric material to serve as a membrane electrolyte in PEFCs. As a polymer with promising mechanical and thermal properties, it is expected to remain chemically stable under high temperature conditions. SF's obtainment methods are already known and optimized by multiple references, [22, 23] and its processing into membranes is relatively easy. [50] The main driving force for the exploration of SF is to help contributing to more sustainability in the materials used as electrolytes in PEFCs.

3. Materials and Methods

This chapter describes the materials and the experimental procedures used in the work. The chapter is divided in four main sections. The first lists all the materials used throughout the work. The second describes the procedures used to obtain the regenerated solution of SF. The third section is reserved for membrane preparation and optimization. Finally, the fourth section is dedicated to the description of the techniques used for the physical and chemical characterization of SF membranes.

3.1. Materials

Bombyx mori silkworm cocoons were kindly provided by the Associação Portuguesa de Pais e Amigos do Cidadão Deficiente Mental, from Castelo Branco, Portugal. Sodium carbonate (Na_2CO_3, 99%), lithium bromide (LiBr, 99%), and sodium chloride (NaCl, 99%) were supplied by Alfa Aesar^{TM}, and used as received. Sulfuric acid (H_2SO_4, 96%) was supplied by Panreac^{TM} and used as received. Sodium hydroxide microprills (NaOH, 99%) and hydrochloric acid (HCl, 37%) were supplied by Sigma-Aldrich^{TM} and used as received. Spectra-Por® cellulose dialysis tubing (molecular weight cut-off of 12-14 kDa) were provided by Spectrum laboratories^{TM} and were rinsed in distilled water for 10 minutes before usage. Dialysis was performed in Millipore-Q water. Silver paint was provided by Agar Scientific^{TM} and used as received. GDL Sigracet 34BC was provided by SGL Group^{TM} and used as received.

3.2. Silk fibroin extraction

The following extraction and purification procedures, reported in the literature, [50,51] were studied in an attempt to choose and optimize one of them.

3.2.1. Procedure A

A general scheme of this procedure is presented in Figure 15. Silkworm cocoons were cleaned and cut into 1 cm^2 pieces. Approximately 5 g of cocoon pieces were degummed by boiling in a 2 L flask filled with a solution of sodium carbonate (Na_2CO_3) in a concentration of 0.02 M for exactly 30 min, for maximum removal of sericin. After rinsing 3 times the fibroin fibers, in 1 L of distilled water for 20 min, the same were placed in a piece of aluminum foil and dried overnight at room temperature (19-25 °C). The obtained fibroin fibers were weighted and suggested a degumming yield of 78%. The next day, the fibers were dissolved in a 9.3 M aqueous solution of LiBr for 4 h at 60 °C, in an oven. After the dissolution was complete, the amber colored solution was placed inside a Spectra/Por® regenerated cellulose membrane tubing with a molecular weight cut-off (MWCO) between 12 and 14 kDa and dialyzed against ultrapure water in a 1 L beaker for 49 h, with six changes of water. The purification procedure was monitored by conductivity measurements until the values were constant and lower than 10 $\mu S.cm^{-1}$.

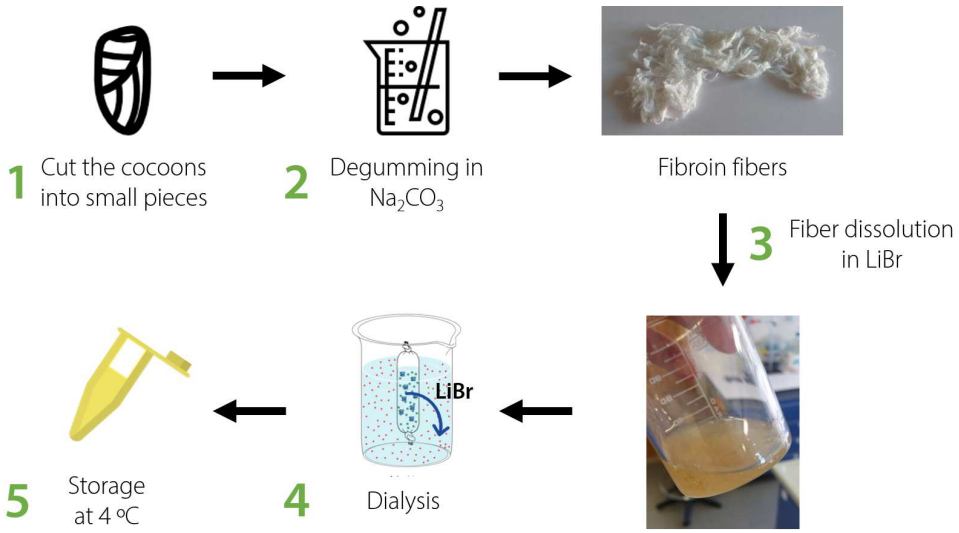

Figure 15 – General schematic of Procedure A.

The obtained solution was centrifuged twice at 4 °C and 12 700 ×G, each time for 20 min, to remove impurities. The regenerated SF solution was stored at 4 °C until usage and presented an average gelation time of 30 days. SF concentration was 4% (m/v), determined by dripping 0.5 mL of solution into a medium weigh boat, followed by solvent evaporation (dry weight method).

3.2.2. Procedure B

A second procedure was studied with the sole purpose of reducing the extraction time of fibroin, which is rather long due to the time consuming dialysis. This procedure is schematically represented in Figure 16.

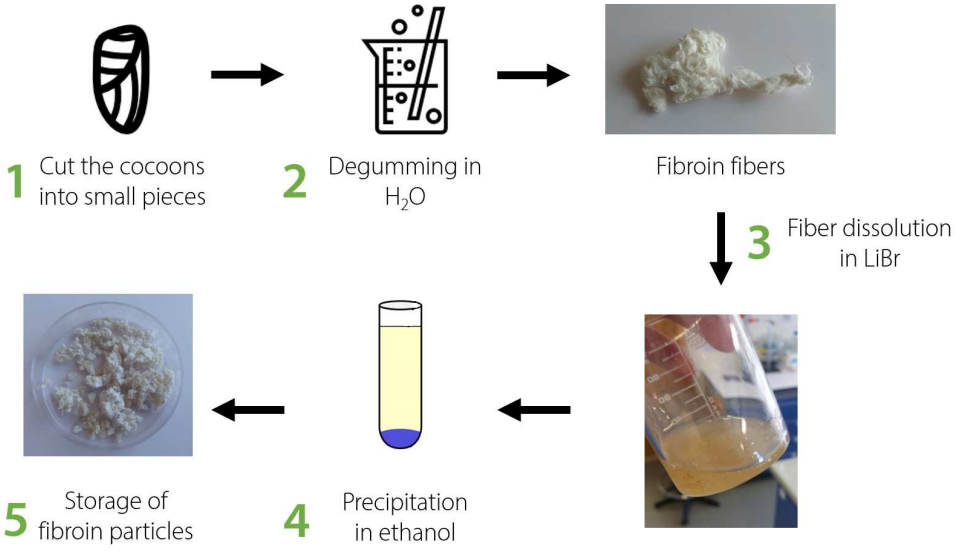

Figure 16 – General schematic of Procedure B.

The *Bombyx mori* cocoons were cut in 1 cm^2 pieces and approximately 5 g of cocoon pieces were weighted. Degumming was performed in a 2 L beaker filled with distilled water for approximately 3 h. After being rinsed 3 times in 1 L of distilled water for 20 min, the fibroin fibers were dried in an oven at 50 °C for about 8 h. The fibers were weighted after drying, and accounted a degumming yield of 85%, which might imply that the degumming procedure was not fully accomplished, since sericin content in *Bombyx mori* silkworm cocoons is around 20-30 wt% . [52]

The dried fibroin fibers were dissolved in a 9.3 M aqueous solution of LiBr for approximately 2 hours and 30 minutes in a 90 °C water bath. The time of dissolution was determined by visual assessment. After performing a filtration with a laboratory funnel to remove the bigger impurities, 5 mL of the obtained amber solution were slowly dripped into a beaker with 150 mL of well-stirred ethanol. This step was repeated until the solution was consumed. When the fibroin solution was dropped into ethanol, fibroin precipitated into small white particles, while the lithium salt remained in solution. After filtration under vacuum of the particles and repeated washes with

distilled water, the particles were dried in the oven at 50 °C for about 2 h and stored in a desiccator.

The original procedure however, does not mention the exact time required for the degumming and dissolution processes, and shows no signs of reproducibility, since the degumming in water for up to 4 hours does not look effective in removing all the sericin present in the cocoons. The boiling in water is probably only efficient in removing the sericin on the outermost layer of the cocoons. Also, the precipitation in ethanol is inconsistent and highly dependent on the dissolution process, since a more viscous solution will not precipitate into small fibroin particles immediately after being dropped into the ethanol solution, as is originally reported. Because of the inconsistency of the procedure, it was thereby discarded, and all the regenerated silk fibroin solution was obtained using Procedure A.

3.3. Membrane preparation

The preparation of the silk fibroin membranes was performed by the solvent casting technique and was went through a process of optimization. Initially, 5 mL of the regenerated SF solution at 4% (m/v) were decanted into a Petri dish (50 mm wide) and the solvent was removed by evaporation at room temperature (19-24 °C) and atmospheric pressure for approximately 3 days. The produced membrane adhered to the Petri dish and therefore its removal was compromised.

Hence, the following membranes were prepared by decanting 5 mL of RSF into polystyrene Petri dishes (50 mm wide) , 2.5 mL of RSF in a teflon custom-made square cavity (about 30 mm wide) and 15 mL in another teflon custom-made square cavity (about 60 mm wide) with the solvent being removed slowly by evaporation at RT. The prepared membranes could be easily removed and therefore the teflon square cavities were chosen, since their geometry allowed the usage of all the available membrane area.

In order to induce crystallization, the membranes prepared at RT in the teflon cavity at atmospheric pressure were placed for 24 hours under 98% relative humidity (RH) at room temperature, using a closed desiccator with saturated water vapor from a potassium sulfate (K_2SO_4) saturated solution. [53] The post-treated membranes (SF-98RH) were kept in this environment as a way to keep control of the storage conditions. The final membrane thickness was 90 µm, measured with a micrometer.

The acid-treated membranes, hereafter named as SF-A, were prepared by immersion of a 98% RH membrane in 60 mL of 0.5 M H_2SO_4 for 24 h. Base-treated (SF-B) membranes were prepared by immersion in 60 mL of 0.005 M NaOH, also for 24 h. A membrane without any kind of post-treatment (SF-R) was kept in a desiccator and used as a reference.

3.4. Physical and chemical characterization

Fourier Transform Infrared Spectroscopy (FTIR)

In this work, IR spectra were obtained in a FTIR Brucker Tensor 27 equipped with an OPUS® (V4.5) software, in the wavenumber range of 4000-350 cm^{-1}, with 256 scans and 4 cm^{-1} resolution. All the samples were placed under the beam without any prior modification. The main motifs for FTIR-ATR usage were to confirm the success of the degumming procedure and to verify any modifications on SF's structure, in particular, changes on the amide I (1600-1700 cm^{-1}) and amide II (1450-1600 cm^{-1}) regions.

X-ray diffraction (XRD)

XRD measurements were performed at room temperature on a PANalytical Empyrean powder diffractometer ($Cu_{K\alpha 1,2}$ X-radiation, λ = 1.542512 Å) equipped with a PIXcel 1D detector and a flat-plate sample holder in a Bragg-Brentano para-focusing optic configuration (45 kV, 40 mA). The patterns were collected in transmission mode using the step-counting method with a step of 0.0261 in the 5-40 2θ range. The main objective of using XRD in this work was to evaluate changes in the crystallinity of SF membranes.

Ion-Exchange Capacity (IEC)

IEC measures the capacity of an insoluble material to displace ions lossely attached to its structure, when placed in a solution containing charged ions. [54]

In this work, pieces of SF-98RH and SF-A membranes were dried at 60 °C for 3 h under vacuum in a Büchi Glass Oven model B-585, weighted, and then immersed in 20 mL of 2 M NaCl for exactly 24 h, to allow the ion-exchange to occur. The membrane pieces were disposed of and the resulting solutions were titrated using a 0.005 M NaOH solution. For these samples, IEC was calculated using Equation 3.1. [55]

$$IEC\,(\frac{mmolH^+}{g}) = \frac{Vol_{NaOH} \times Conc_{NaOH}}{W_{dry}} \tag{3.1}$$

Where Vol_{NaOH} is the volume of NaOH corresponding to the equivalence point, $Conc_{NaOH}$ is the concentration of the sodium hydroxide solution and W_{dry} is the dry weight of the membrane piece, before being immersed in NaCl.

The membrane immersed in base, SF-B, was also dried at 60 °C for 3 h under vacuum, weighted, and then immersed for 24 hours in 50 mL of 0.01 M HCl. The resulting solution was titrated using a 0.01 M NaOH solution. IEC, however, was calculated using Equation 3.2. [55]

$$IEC\,(\frac{mmolH^+}{g}) = \frac{Conc_{HCl} \times Vol_{HCl} - Conc_{NaOH} \times Vol_{NaOH}}{W_{dry}} \tag{3.2}$$

Where Vol_{NaOH} and Vol_{HCl} are the volume of NaOH corresponding to the equivalence point and the used volume of HCl, respectively, $Conc_{NaOH}$ and $Conc_{HCl}$ are the concentrations of the solutions and W_{dry} is the dry weight of the membrane piece, before being immersed in HCl.

In all titrations, the pH was monitored using a Eutech Instruments^{TM} pH 110 Cyberscan.

Swelling and water up-take

Room temperature and dry conditions do not reflect the real PEFC operating conditions, which can vary up to high temperatures and high relatives humidities. These parameters have a big influence on PEFC's components, namely on the membrane electrolyte, since different working conditions affect the membrane's mechanical and electrical properties. [56] At higher relative humidities, the polymer electrolyte will up-take more water, and can therefore swell, applying pressure to the catalyst and gas diffusion layers. Thus, it becomes important to understand how the material behaves in terms of water up-take and swelling ratio.

Water up-take and swelling studies were conducted by drying pieces of the prepared membranes at 60 °C for 3 hours under vacuum, weighing them in an analytic scale (W_{dry}), and measuring their thickness with a micrometer (h_{dry}). They were then placed in 40 mL of distilled water for exactly 24 hours. After cleaning them with absorbing paper to remove excess water, the weight (W_{wet}) and thickness (h_{wet}) were once again determined. Water up-takes and swelling ratios were calculated using Equation 3.3 and

Equation 3.4, respectively. [57]

$$W_{up}\,(\%) = \frac{W_{wet} - W_{dry}}{W_{dry}} \times 100 \tag{3.3}$$

$$Swelling\,ratio = \frac{h_{wet} - h_{dry}}{h_{dry}} \tag{3.4}$$

Scanning Electron Microscopy (SEM)

SEM is one of the most interesting techniques to be performed, since it allows analysis of the surface details down to nano-scale and giving a direct insight on the morphology, topography and composition of the materials. Unlike conventional light microscopy, SEM works by sending an electron high energy beam that sweeps the sample. The interaction between the beam and the sample produces secondary electrons and X-rays. While the mapping of the intensities of these electrons produce images that allow morphological analysis, the sample characteristic X-rays can be used to perform Energy-dispersive X-ray spectroscopy (EDS), thus allowing the local elemental analysis and/or a composition mapping of the sample's surface. [58] It's important to be aware that the more voltage the beam has, more probable is for sample degradation to occur. Also, it is mandatory to ensure conductivity through the sample's surface, which can be done by carbon-deposition (or gold). [58]

In this work, SEM is useful for analyzing the morphology of the prepared SF membranes of their topside, backside, and cross-sections. The results of the degumming process can also be observed in SEM, since the sericin layer around fibroin disappears between the cocoons and the fibroin fibers. These analysis were performed using a Hitachi SU-70 microscope equipped with a Brucker Quantax 400 detector for EDS. All the samples were previously coated with a thin layer of conductive carbon. 15kV of voltage was used.

Dynamic mechanical analysis (DMA)

DMA was used in this work to measure the viscoelastic properties of rectangular pieces of the SF membranes (30 × 5 mm^2). The analysis was performed on a Tritec2000 DMA (Triton Technologies) operating in tension mode (single strain) at 0.1 Hz and 1 Hz, with a 0.01 mm displacement. The temperature range was varied from -100 to 220 ºC with a constant heating rate of 2 °C.min^{-1}.

Thermogravimetric analysis (TGA)

TGA gives information about the weight loss or gain of the samples due to decomposition, oxidation or dehydration. The main usage of the technique is to clarify the thermal stability of the material, which can be done to up to 1200 °C. [59]

This analysis was performed to evaluate the thermal stability of SF membranes. TGA was performed on a Setsys Ev 1750 (Seteran^{TM}) thermal analyzer under a nitrogen flow of 200 mL.min^{-1}, from 25 °C to 800 °C with a 10 °C.min^{-1} heating rate.

Tensile tests

In this work, tensile assays were performed to evaluate the mechanical properties of the SF membranes. Tests were performed on a Instron^{TM} model 5966 testing machine equipped with Bluehill software (V3.0) in tensile mode with a cross-head velocity of 10 mm.min^{-1} and a load cell of 500 N. The samples were strips of average 60 mm × 5 mm and the gauge length was 30 mm. 3 to 6 specimens were tested, depending on each sample, and the average value was recorded.

Gel permeation chromatography (GPC)

In this work, GPC was used with the intent of determining the molecular weight of the regenerated solution of 4% (m/v) fibroin and to evaluate degradation resulting from the addition of H_2SO_4 or NaOH to the SF solution. The technique was performed on a PL-GPC 110 (Polymer Laboratories^{TM}) equipped with a refractive index detector. The calibration was performed with a glucose reference and the used eluent was Lithium Chloride.

Dynamic vapor sorption (DVS)

DVS is a well-established method for the determination of vapor sorption isotherms and measures uptake and loss of vapor gravimetrically using a ultramicrobalance. The high mass resolution and stability allows the instrument to measure the adsorption and desorption of very small amounts of water. The vapor partial pressure (relative humidity) around the sample is controlled by mixing dry and saturated gas streams with the help of mass controllers, while the temperature is maintained constant. [60]

DVS measurements were performed on a DVS resolution dual vapor analyzer (Surface Measurement Systems^{TM}), at 25 °C and from 0 to 98% RH, with steps of 10% RH up

until 70% RH, and steps of 5% RH until 98% RH. Both the sorption and desorption curves were recorded.

Impedance Spectroscopy (IS)

The technique consists on the application of an electrical potential on the material (V), under the form of a sine wave (Equation 3.5).

$$V = V_0 \times e^{i\omega t} \tag{3.5}$$

This potential will generate an electrical current in the material as a response, also in the form of a sine wave (Equation 3.6). However, this response will come with a phase angle, δ, corresponding to the phase difference between the applied potential and the resulting electrical current. [61]

$$I = I_0 \times e^{i\,(\omega t + \delta)} \tag{3.6}$$

Where V_0 and I_0 are the maximum amplitudes of V and I, respectively, ω is the angular frequency in rad.s^{-1} and t is the time (seconds). By making an analogy with Ohm's law, one can define the impedance Z of the material (Equation 3.7). [62]

$$Z = \frac{V_0}{I_0} \times e^{i\delta} = Z_0 \times e^{i\delta} \tag{3.7}$$

Z can be represented in the complex Argand's plane, according to Equation 3.8.

$$Z\,(\omega) = Z^{'}\,(\omega) + iZ^{''}\,(\omega) \tag{3.8}$$

Where $Z^{'}$ and $Z^{''}$ are the real and imaginary components, respectively, while $i = \sqrt{-1}$. Impedance spectra consist on a series of points, representing the magnitude and direction of the impedance vector for a particular frequency, generally from a few mHz to MHz. Another representation of the applied signal response is the Bode diagram, where the impedance's modulus or the phase angle are represented against the frequency.

A pure resistance (R) is represented as a point in the real axis of impedance, because $Z = R$ and $\theta = 0$, while a capacitor (C) or an inductor (L) have contributions only in the impedance's imaginary axis. Their impedance can be described by Equations 3.9, 3.10 and 3.11, respectively. [63]

$$Z_R = R \tag{3.9}$$

$$Z_C = \frac{1}{i \times \omega \times C} \tag{3.10}$$

$$Z_L = i \times \omega \times L_i \tag{3.11}$$

In this work, impedance spectroscopy was used as a way of determining the conductivity of the prepared membranes at various temperatures and relative humidities. Also, and in order to uncover the orientation in which SF membranes have higher values for conductivity, two different sample-holders with different geometric configurations were used, in-plane (IP) and through-plane (TP), represented in Figures 17 and 18, respectively. Membranes with an average length of 1 cm (for IP) and average circular area of 0.5 cm^2 (for TP) were painted with silver electrodes and left to dry for one day. Also, and in order to promote both gas diffusion and better electrical contact with the platinum or silver wires used to connect the sample-holder to the measurement system, the membranes were placed between two carbon cloth layers (working as GDL) and graphite plates with gas channels (only in TP). The sample-holders used a pseudo-4-electrode configuration, as it can be also seen in Figures 17 and 18.

In order to calculate the conductivity (σ), Equations 3.12 and 3.13 were used for both IP and TP, respectively. These equations take in account the resistance, determined from the impedance spectroscopy measurements, and the geometry of each configuration.

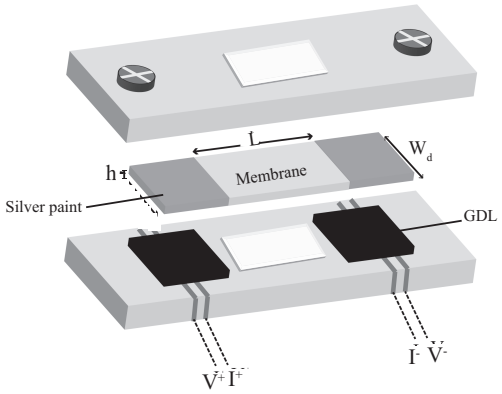

Figure 17 – Schematic of the IP sample holder used in the impedance spectroscopy measurements.

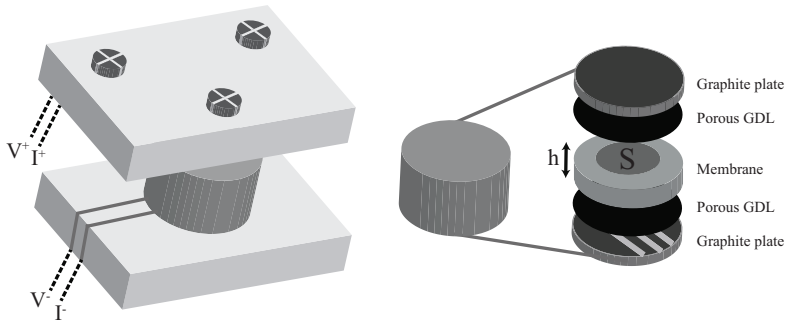

Figure 18 – Schematic of the TP sample holder used in the impedance spectroscopy measurements.

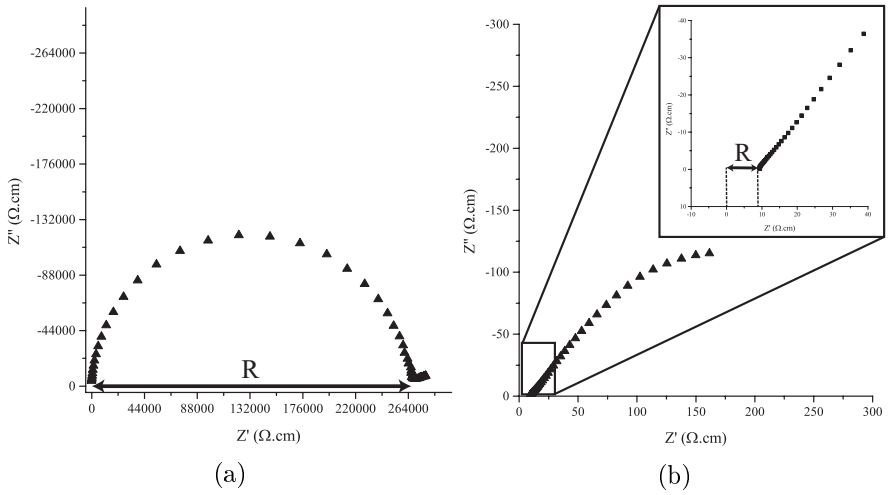

Figure 19 – Nyquist plots obtained for the SF-98RH membrane at 94 °C and 98 %RH. Figure (a) is for the IP results while Figure (b) is for TP.

$$\sigma = \frac{1}{R} \times \frac{L}{W_d \times h} \tag{3.12}$$

$$\sigma = \frac{1}{R} \times \frac{h}{S} \tag{3.13}$$

Where L, W_d, and h are, respectively, the length, width and thickness of the membrane, while S is the electrode's area. All the dimensions are measured about six times in order to obtain an average value before the sample is placed on the sample holder.

The value of resistance is obtained from the Nyquist plots. These will differ the most mainly between low and high values of RH, but will also differ between different geometrical configurations (at the same conditions), due to the difference in thickness and in the conductive path area. In Figure 19, a Nyquist plot with two different spectra is shown.

For IP measurements, the value for resistance can be obtained by the intersection of the semi circle in the Nyquist plots with the real axis, as it can be seen in Figure 19a. However, it can also be seen in this Figure that the electrode part starts at the end of the semi-circle. At higher temperatures, the relaxation frequency increases, and the first semi-circle tends to dissapear to give place to the electrode's behaviour. In these cases, the value for resistance is correspondant to the value of Z' with the minimum Z'', located between the two contributions. [62]

In TP measurements, the high area S and the relatively low value for membrane thickness produce low resistance values, which coupled to a low capacitance, results in relaxation frequencies out of the measuring range of the instrument . This will result in a Nyquist plot that no longer shows the semi circle and only shows the electrode behavior. In this case, the value for resistance is also obtained by the value of Z' at the minimum Z''. The TP measurements are much more affected by errors introduced by the instrumentation in the high frequency range, and therefore one should take special care in the analysis of the obtained impedance spectra.

Impedance spectroscopy measurements were conducted using an Agilent E4980A precision LCR meter in an ACS DY 110 climatic chamber with temperatures from 30 °C to 94 °C and relative humidities from 20% to 98%, using humidity steps. The platinum or silver cables were connected to the LCR meter. Impedance spectra were collected from 20 Hz to 2 MHz with a test signal amplitude of 100 mV, and were analyzed using Zview Software (V2.6 b, Sribner Associates^{TM}).

4. Results and Discussion

In this chapter, the main results of this work are presented and interpreted in an attempt to comprehend how SF can be used as a material for novel, sustainable polymer electrolytes. The chapter is divided in six sections. The first addresses degumming general remarks and analysis of the obtained RSF solution. The second discusses membrane preparation and the post-treatments applied to such membranes, and aims to understand the influence of this post-treatment on SF's structure, through the physical and chemical characterization of the obtained membranes. The third section is dedicated to the water sorption and up-take results obtained for SF membranes and their discussion. The fourth section addresses the thermal analysis results of the membranes, while the fifth section addresses their mechanical properties. The six and last section discusses the results obtained in IS, and attempts to relate them to the structure of SF and to the conditions the membranes were submitted to.

4.1. Degumming and RSF solution

The success of the degumming operation was evaluated by FTIR-ATR analysis and SEM. Figure 20 compares the obtained spectra for the silkworm cocoons with spectra of the fibroin fibers.

Sericin characteristic vibrations can be detected by the bands around 1398 cm^{-1} and 1053 cm^{-1}, in the silkworm cocoons FTIR-ATR. The first band is attributed to the C-H and O-H bending vibrations, while the second band is usually assignable to C-OH stretching vibrations. These absorptions are attributed to the side chains of the amino acid serine, which is more abundant in silk sericin than in SF. [26] However, since SF also has the amino acid serine in its composition, these bands will never disappear completely from the infrared spectra.

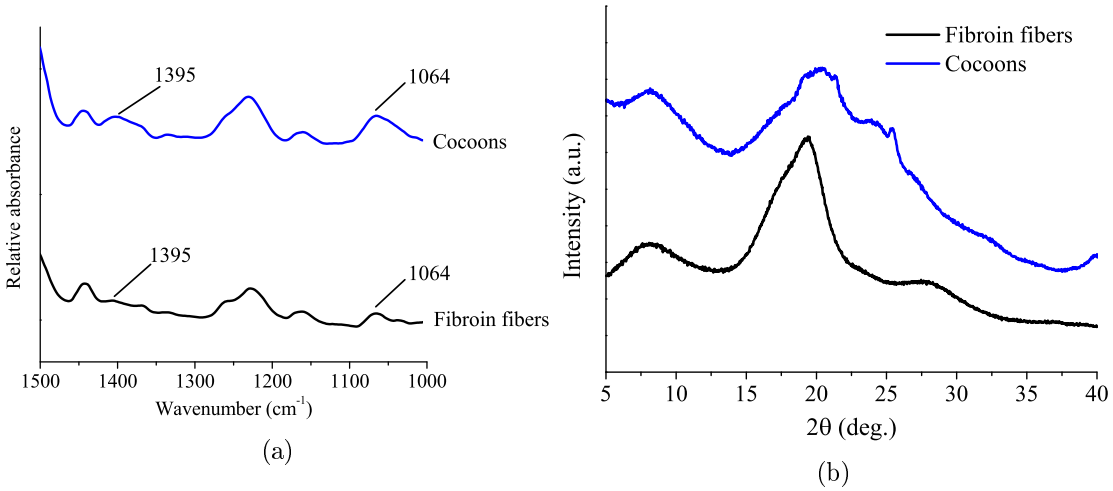

Figure 20 – Infrared spectra of the raw *Bombyx mori* cocoons and of the fibers obtained after degumming.

In XRD, as expected, the diffraction patterns before and after degumming are similar, due to the fact that sericin is amorphous. In fact, the reflexion around 20° is broader for the cocoons, indicating a more amorphous component.

In SEM analysis, degumming is easily verified by comparing images of the silkworm cocoons and of the fibroin fibers, as it is presented in Figure 21.

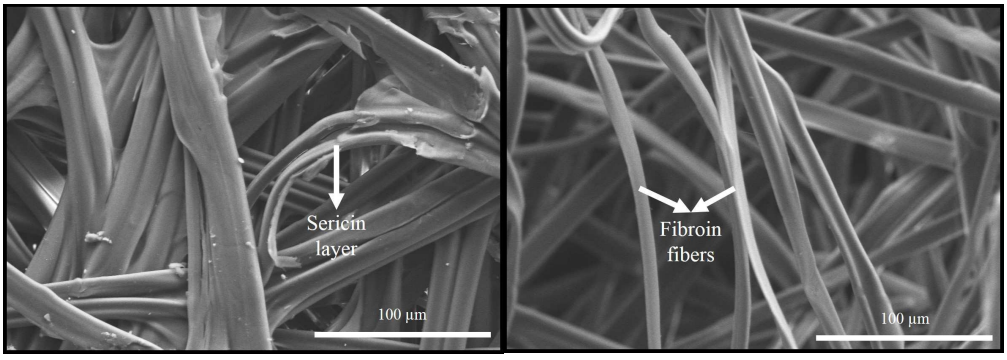

Figure 21 – SEM images of (a) *Bombyx mori* silkworm cocoons and of (b) obtained fibroin fibers after degumming.

As it can be seen, the sericin layer, generally wrapped around two fibroin fibers, disappears, indicating that the degumming procedure was successful in removing all of the sericin.

In order to obtain a value for the average molecular weight of the regenerated silk fibroin solution, GPC was used. The calibration curve obtained is presented in Section A.4 and the obtained chromatogram is presented in Figure 22.

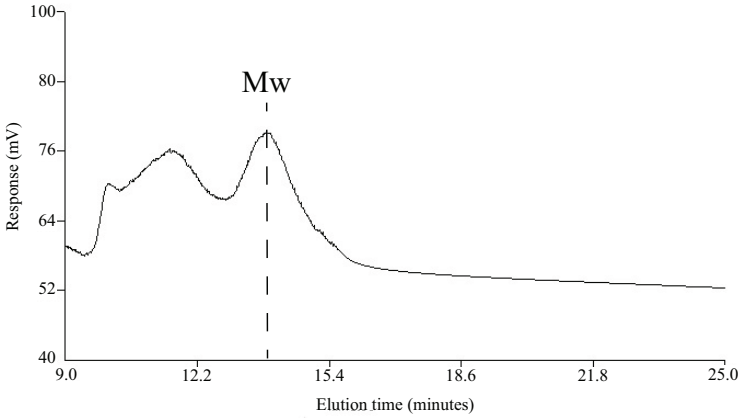

Figure 22 – Obtained chromatogram of the silk fibroin solution.

Based on the indication that the molecular weight of SF ranges from 200 to 350 kDa, as mentioned in the Introduction, the peak around 13.8 min of elution time was considered to be attributed to the molecular weight of the silk fibroin solution, whilst the broad peaks between 9.5 and 11 min of elution time are thought to be associated with aggregates. By using the calibration curve equation with the value of 13.8 min, the obtained value for M_w is 202 227 g.mol^{-1}.

4.2. Structure and microstructure of the SF membranes

As described in the Materials and Methods chapter, the SF membranes were prepared by the solution casting technique. For the sake of optimizing this procedure, membranes were cast at room temperature (*ca.* 21 °C), 40 °C and 60 °C, under normal atmosphere. The obtained FTIR-ATR and XRD results are presented in Figure 23. In the IR spectra of SF membranes, the amide I and amide II regions are usually the ones of interest, because the conformation of SF will influence the position of the bands in these regions. The Silk I structure of SF and the random coil structures exhibit the typical absorption bands around 1650 cm^{-1}, while Silk II shows the characteristic absorption bands around 1697, 1622 and 1518 cm^{-1}. [64] Membranes were also prepared under vacuum, at different temperatures, but the high rate of water evaporation yielded membranes with heterogeneous thickness due to the formation of bubbles. The IR spectra of these membranes are presented in Figure A.2, and these spectra are very similar to the ones presented by membranes prepared at atmospheric pressure.

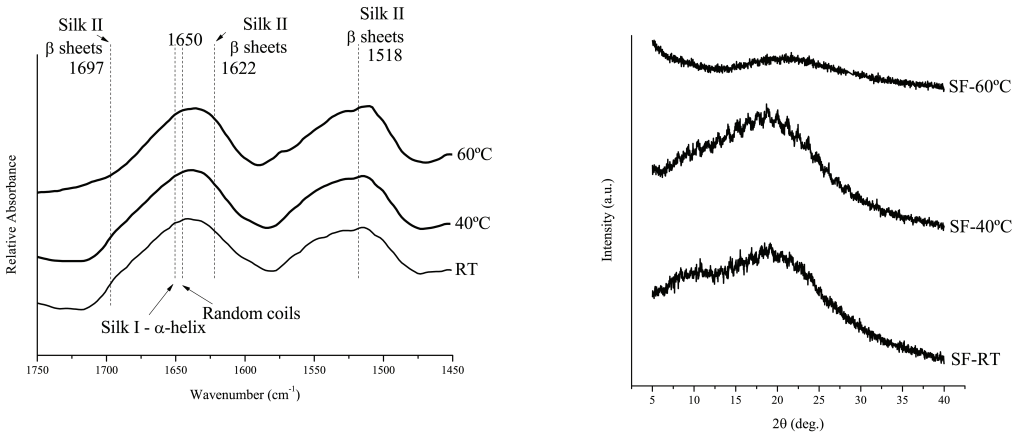

(a) (b)

Figure 23 – (a) FTIR-ATR and (b) XRD results of the membranes prepared by casting of the RSF solution, at different temperatures.

The IR and XRD results of all the membranes prepared suggested an amorphous structure. As a result, all of the SF membranes prepared behaved poorly after being placed in distilled water, shrinking and ultimately dissolving, as it can be seen in Figure 24.

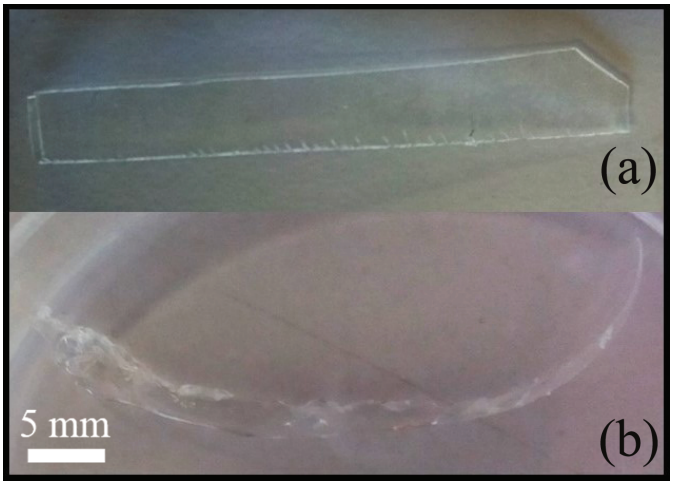

Figure 24 – Images of a initially prepared membrane (a) before and (b) after the addition of water, showing its shrinking behavior.

SEM analysis was performed on the SF membranes prepared at different temperatures. The images of the membrane prepared at room temperature are presented in Figure 25 while the other SEM images are presented in Figures A.3 and A.4. The images show that when the temperature increases, water evaporates faster, influencing the morphology of the prepared membranes.

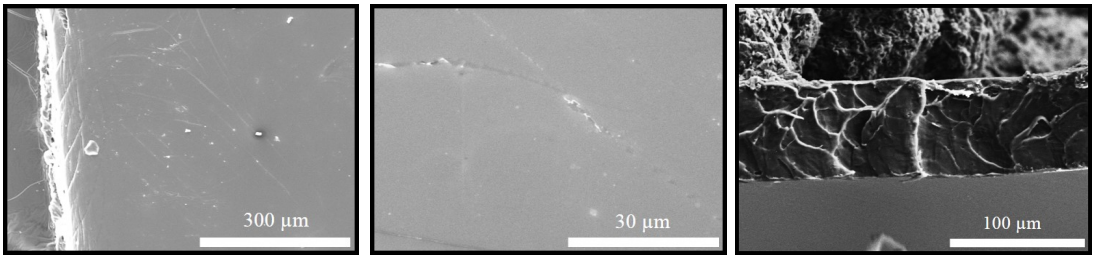

(a) (b) (c)

Figure 25 – SEM images of the prepared membrane at RT. Picture (a) is the top side of the membrane (b) the bottom side and (c) the cross-sectional view.

The membrane prepared at room temperature is homogeneous throughout its surface, unlike the membranes prepared at higher temperatures, that, due to the rapid evaporation of water, end up with less homogeneity.

EDS was performed to check if there were any traces of LiBr that could be affecting the self-assembly of SF, producing membranes with less crystalline content. The results are presented in Figure 26. Traces of iron were found at the surface of some of the membranes, and this component is generally associated to the impurities of comercial LiBr, but there was no indication of LiBr traces that could be affecting the membrane structure. [65]

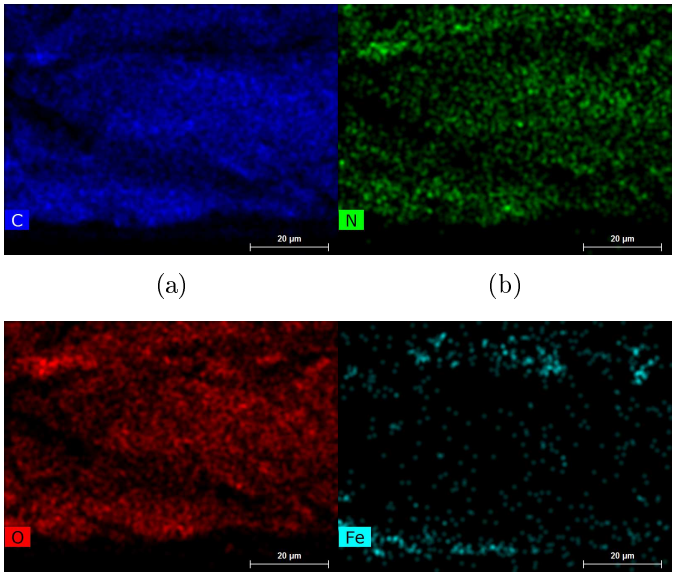

(a) (b)

(c) (d)

Figure 26 – EDS mapping of the cross-sectional view of the membrane prepared at RT. There can be seen traces of iron (d), but the composition is mainly carbon (a), nitrogen (b) and oxygen (c).

It was later acknowledged that the lack of stability in water and the indications of an amorphous structure in FTIR-ATR and XRD is a consistent result of membranes

prepared from the regenerated solution of SF. This is a consequence of fiber dissolution with LiBr. The latter acts as a swelling agent, breaking the hydrogen bonding in the crystalline structure of the fibroin fibers and eventually reducing the molecular weight of SF. [66] The molecular weight of the fibers could not be determined by GPC due to difficulty in dissolving them in the recommended solvents (Water, Dimethylacetamide, Dimethylformamide or Lithium Chloride).

Hence, all the membranes prepared from the regenerated silk fibroin solution will have a lower content of Silk II, demonstrating an amorphous structure and water solubility. [65]

After these results, the membrane prepared at RT was used for all further studies as reference (SF-R), since it demonstrated a more homogeneous surface in SEM and took more time to be prepared due to the slower solvent evaporation. This might suggest that if the membrane underwent self-assembly, it was more extensive than for the membranes prepared at 40 °C and 60 °C.

Stability in water is important when the desired application is as a membrane electrolyte, since ion conduction requires water and therefore processes for obtaining stronger, water-insoluble SF membranes were studied. In order to obtain such properties, the generally used approach is to perform post-treatments on the membranes after their casting or prepare membranes by slower drying, to increase the amount of the Silk II fraction of the structure (β-sheet formation) by the rearrange suggested in Figure 13.

Slower drying can produce stronger and water-insoluble membranes, because the time for self-assembly increases, but this method is easily influenced by several factors, such as room temperature or chosen membrane thickness. [65] Membranes produced by casting usually have a maximum β-sheet crystallinity of 14%, [64] while membranes prepared by slow drying have β-sheet crystallinity of about 23.2% [65] Treatments with methanol/ethanol (immersion or annealing) and steam autoclaving are the most widely used and are known to produce membranes with β-sheet crystallinity between 52 and 60%, although very brittle and with a low capacity for elongation. [64]

In order to obtain strong but less brittle membranes for increased mechanical properties, other post-treatment options were researched. Recent studies have proposed methods for inducing β-sheet formation in SF membranes, but to an extent at which the membranes are insoluble in water, relatively strong, and not so brittle as the alcohol treated or steam autoclaved membranes. [53,64] These treatments consist on placing the membranes under higher RH, where bound water will disrupt the intermolecular forces between protein

chains, promoting the movement of the non-crystalline regions and the aggregation of the hydrophobic parts of the structure through helix-helix interactions, which is suggested to occurr within the micellar structures proposed in Figure 13. [53, 67] The degree of crystallinity induced by this post-treatment is reported to be around 40% [53]

In this work, the RH of 98% was chosen, since it is reported to produce strong membranes with elongation at break. [53] The chosen value for RH approaches saturation and therefore immersion in water was also attempted to see if similar results would be obtained. FTIR-ATR and XRD data collected on the initial and post-treated membranes are presented in Figure 27. The XRD patterns of SF membranes show a broad band at about $2\theta = 20°$. The intensity of this band decreases when the crystallinity of SF decreases. [68] The characteristic diffraction peaks of the Silk I structure are at $2\theta = 12.2°$, 19.7°, 24.7°, 28.2°, 32.3°, 36.8°, and 40.1°, while the Silk II structure has reflexions at 2θ values of 9.1°, 18.9°, 20.7°, and 24.3°. [69, 70]

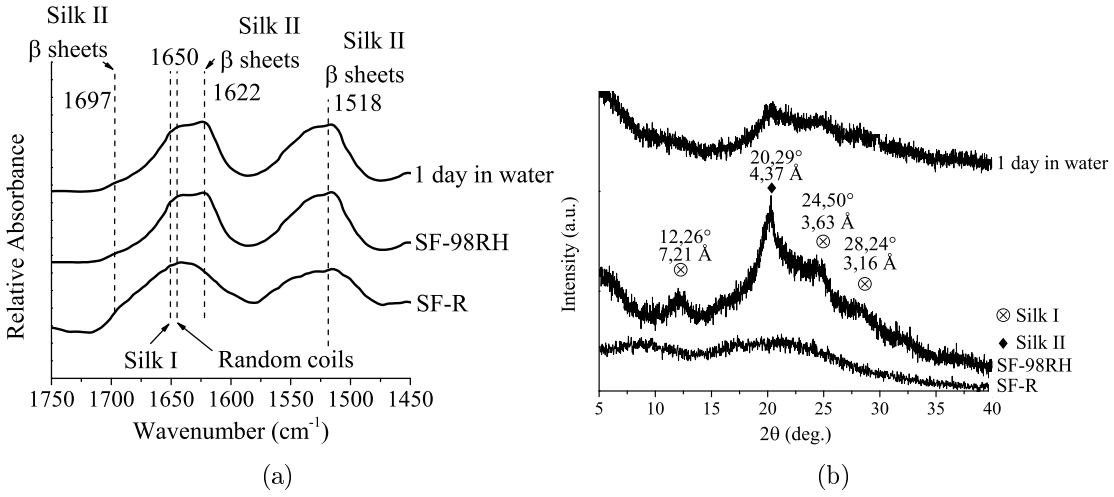

Figure 27 – (a) FTIR-ATR and (b) XRD results of the cast SF membrane and the comparison between the treatment at 98% RH for 1 day and by immersion in water for 1 day.

A coexistence between the Silk I, random coil and Silk II structures is seen in both the procedures, confirming that both these treatments allow the rearrange in SF's structure and posterior increase in crystallinity. [53] XRD data in Figure 27b shows that the membrane treated at 98% RH for 1 day (SF-98RH) shows more intensity at the characteristic band of the Silk II structure, therefore suggesting this treatment produces higher crystallinity than immersion in water. The stability in water of the membrane treated at 98% RH was also higher.

In order to study the influence of treatment time and membrane thickness on the extent of crystallization, the SF-98RH membrane and a thicker membrane, also prepared by

solution casting at RT for 3 days (150 µm), were kept under 98% RH for 15 days, and were monitored by FTIR-ATR and XRD. The evaluation was performed for a maximum of 15 days, and the FTIR-ATR spectra collected are presented in Figure 28.

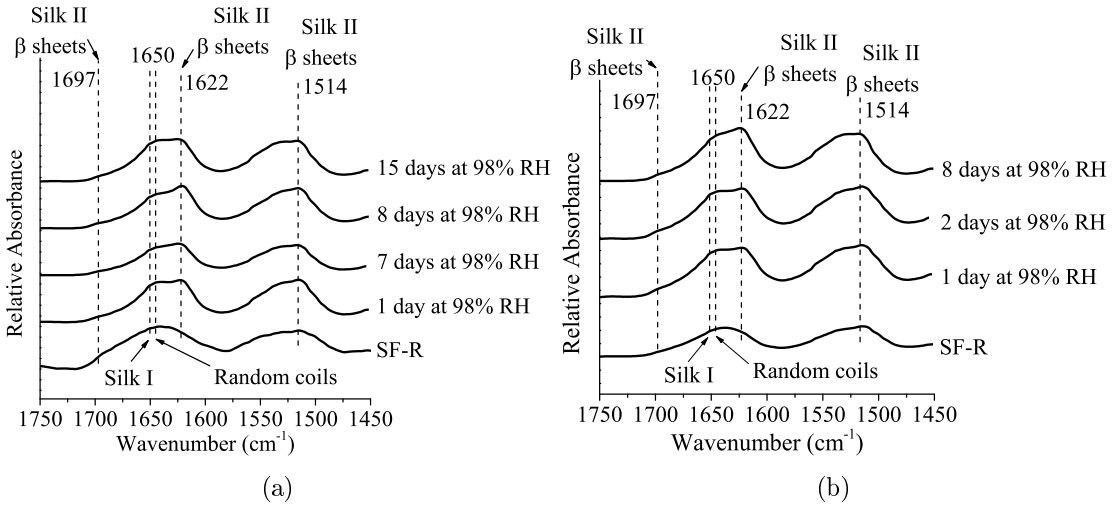

Figure 28 – FTIR-ATR results of (a) 90 µm membrane submitted to 98% RH for up to 15 days and for (b) 150 µm membrane submitted to the same treatment for 8 days.

The obtained IR spectra suggest that the crystallization-inducing treatment at 98% RH does not vary significantly for up to 15 days, which means that membranes can be kept in such environment, as a way to maintain the same "history" for all the prepared membranes. The results were also confirmed by XRD (Figure 29). Thickness is apparently also a non-factor when it comes to post-treatment efficiency and FTIR-ATR confirmed that the thicker membrane also transitioned to the Silk II structure after only 1 day of post-treatment.

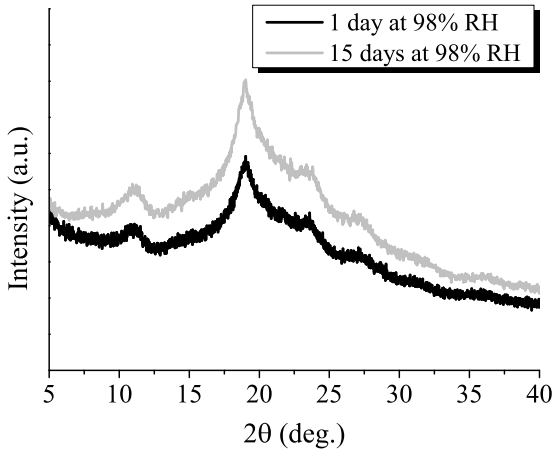

Figure 29 – X-ray diffraction patterns comparing 1 day with 15 days of post-treatment. One can see there is no difference.

FTIR-ATR and XRD analysis were performed to confirm that the SF-98RH membrane structure remains unaltered after being dried under vacuum at 60 °C (Figure 30). The results suggest that the membranes can be dried in such conditions after being treated at 98% RH, if such is needed, because there was no apparent structural change that would somehow show structure reversibility.

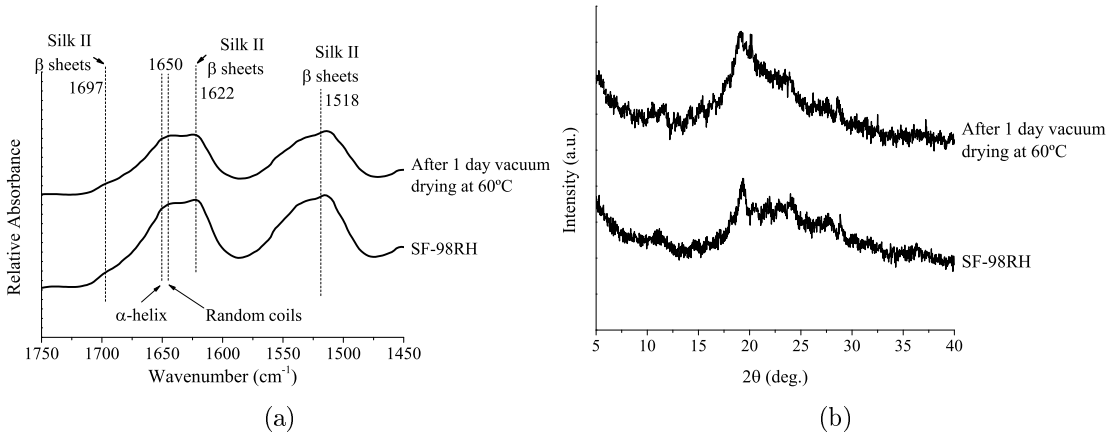

Figure 30 – (a) FTIR and (b) XRD results of the SF-98RH membrane before and after being dried under vacuum at 60 °C.

In order to be used as an electrolyte, SF has to be able to endure aggressive environments, such as acidic and alkaline, which are generated when positive or negative species are being conducted. In order to evaluate the chemical stability of the SF-98RH after being placed in acid and alkaline media, the SF-A and SF-B membranes were evaluated by FTIR-ATR and XRD. The results are presented in Figure 31.

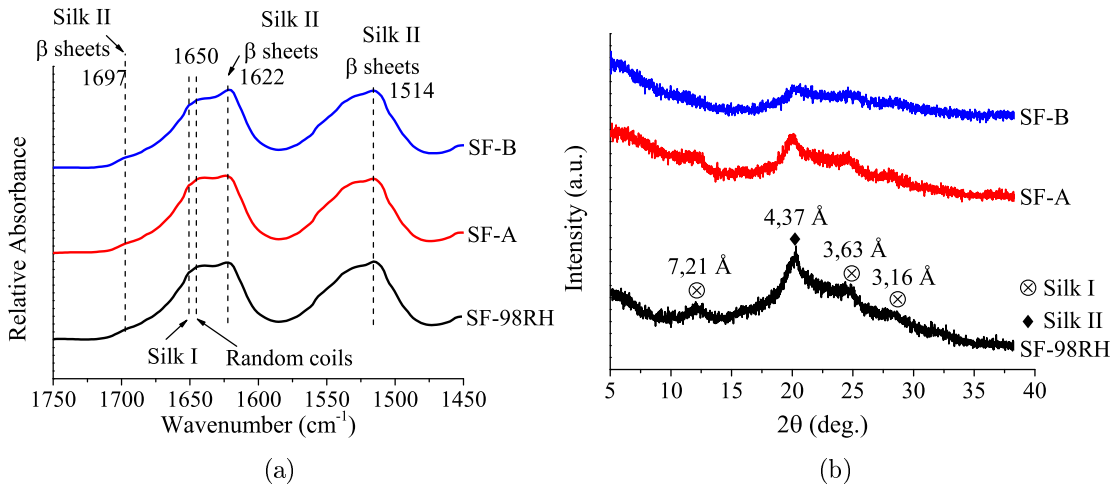

Figure 31 – (a) FTIR-ATR and (b) XRD results comparing the SF-98RH membrane with the acid and base treated membranes.

The obtained FTIR-ATR spectra do not show any signs of change in the structure of

SF. However, XRD results show an apparent decrease in crystallinity for the acid and base-treated membranes, which could suggest some hydrolysis taking place. The initial tests that dictated the usage of a 0.005 M concentration of NaOH (pH=12) showed that at pH>12, SF was completely degraded.

In order to attempt the confirmation of hydrolysis taking place, GPC was used to evaluate the decrease in the molecular weight of SF after the acid and alkaline treatments. Since the membranes could not be dissolved in any of the recommended solvents (Water, Dimethylacetamide, Dimethylformamide or Lithium Chloride), the analysis was performed by mixing the SF solution in a 3:1 (v/v) proportion with both the acid and alkaline solutions with in the treatments. The resulting chromatograms are presented in Figure 32.

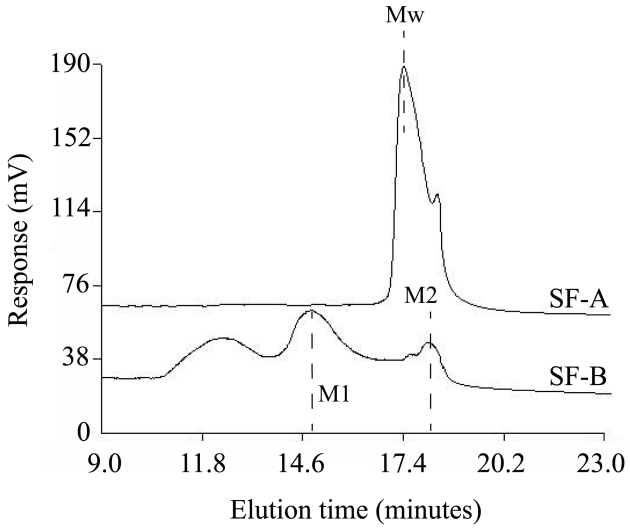

Figure 32 – Obtained chromatograms of SF-A and SF-B.

Based on the fact that the molecular weight of these samples should be equal or lower than the molecular weight of the RSF solution, the peaks attributed to the molecular weight of SF-A and SF-B are assigned in the Figure. After using the calibration curve for the calculations, the SF-A sample returns a value for M_w of 676 g.mol^{-1}, implying a very high decrease in the molecular weight of SF. The base treated sample shows two values for the molecular weight, M_1 and M_2. The first has a value of 41686 g.mol^{-1}, while the second has a value of around 263 g.mol^{-1}. Both values also show a decrease in the molecular weight of SF after the alkaline treatment. However, since the GPC was not performed for the dissolved membranes but for the SF solution mixed with both the acid and alkaline solutions, it cannot be thoroughly inferred that hydrolysis takes place when the SF-98RH membrane is immersed in the acid and/or alkaline solutions, but still gives

an indication that it could be happening, since the regenerated SF solution undergoes degradation when mixed with H_2SO_4 and NaOH in the same concentrations used on the membranes.

As a follow-up to the acid and basic treatment, the ion-exchange capacity of the membranes was evaluated, so it would be possible to understand the influence of the acid and base treatment on the capacity of the structure of SF to lose attached protons. IEC values are presented in Table 2. These values were determined from the titration curves presented in Figure A.5. The IEC value for SF-R could not be calculated from the obtained titration curve because there was no visible equivalence point.

Table 2 – Ion-exchange capacity values of the prepared membranes.

Membrane	IEC (mmol $H^+.g^{-1}$)
SF-R	–
SF-98RH	0.44
SF-A	0.015
SF-B	0.011

The highest value for IEC was determined to be for the SF-98RH membrane, while SF-A and SF-B afforded much lower values. This is suggested to be due to the fact that the ordered micellar structure formed by SF after crystallization has very acidic hydrogen atoms in its hydrophilic surface, mainly due to the -OH side groups of the amino acid serine. These acidic hydrogen atoms are available for being exchanged with the Na^+ ions of the NaCl solution used in the procedure.

When the membrane is treated with the acid or the base, the hydrophilic surface of the protein is most probably disrupted, and the available number of acidic hydrogen atoms decreases significantly, translating in lower IEC values. This might be another indication that the acid and base treatments may have a negative impact on the performance of SF membranes. IEC determinations were also not repeated to confirm all the obtained results, and therefore an error on these calculus can not be presented and is therefore acknowledged has a possible future task.

In order to evaluate the influence of the post-treatment at 98% RH and of the acid and base treatments on the membranes, SEM images of the SF-98RH, SF-A and SF-B membranes are presented in Figure 33.

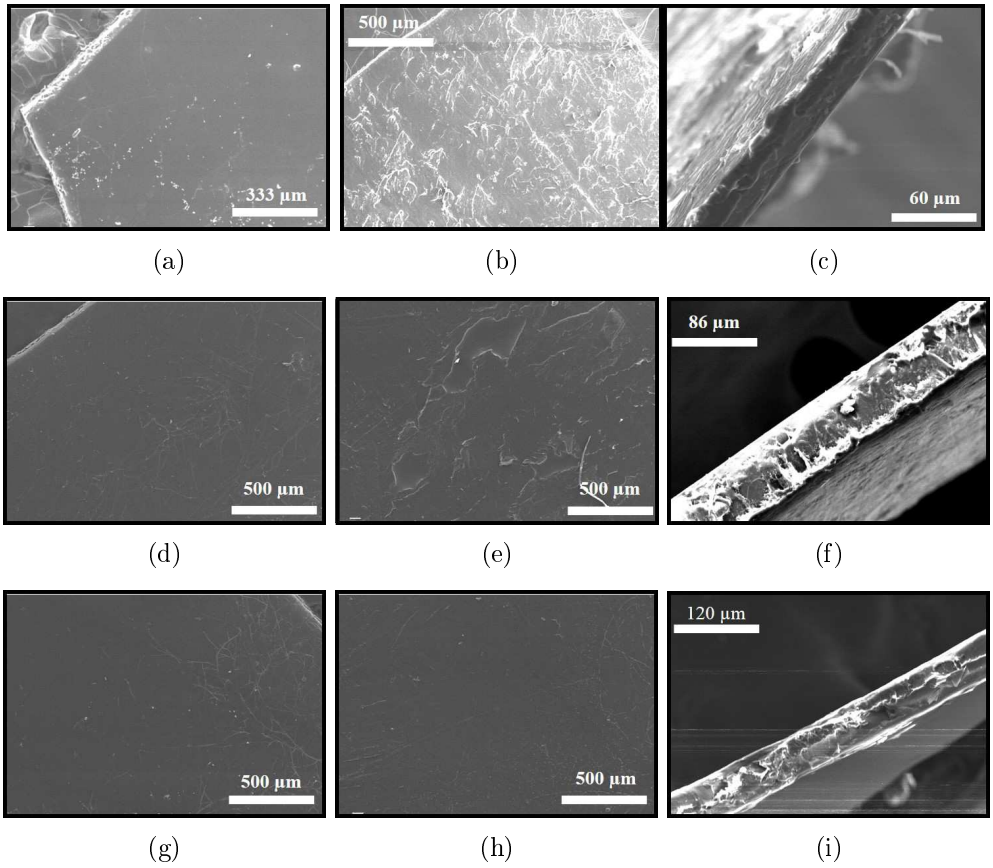

Figure 33 – SEM images of the SF-98RH, SF-A and SF-B membranes: (a) are the top side of the membranes (b) the bottom side and (c) the cross-sectional view.

The SF-98RH seems to have a less homogeneous surface in relation with the SF-R membrane, especially on the bottom side. This is suggested to be a result of the influence of water on the surface of the membrane. SF-A is also less homogeneous on the bottom side, probably due to a similar effect. The SF-B membrane however, has a more homogeneous appearance.

4.3. Water uptake and sorption

Since water content and swelling ratio have a big influence on the ion conducting capability of membrane electrolytes and on the normal functioning of the PEFC, it becomes highly important to evaluate and discuss these properties.

The obtained water vapor sorption isotherms of all the membranes are presented in Figure 34.

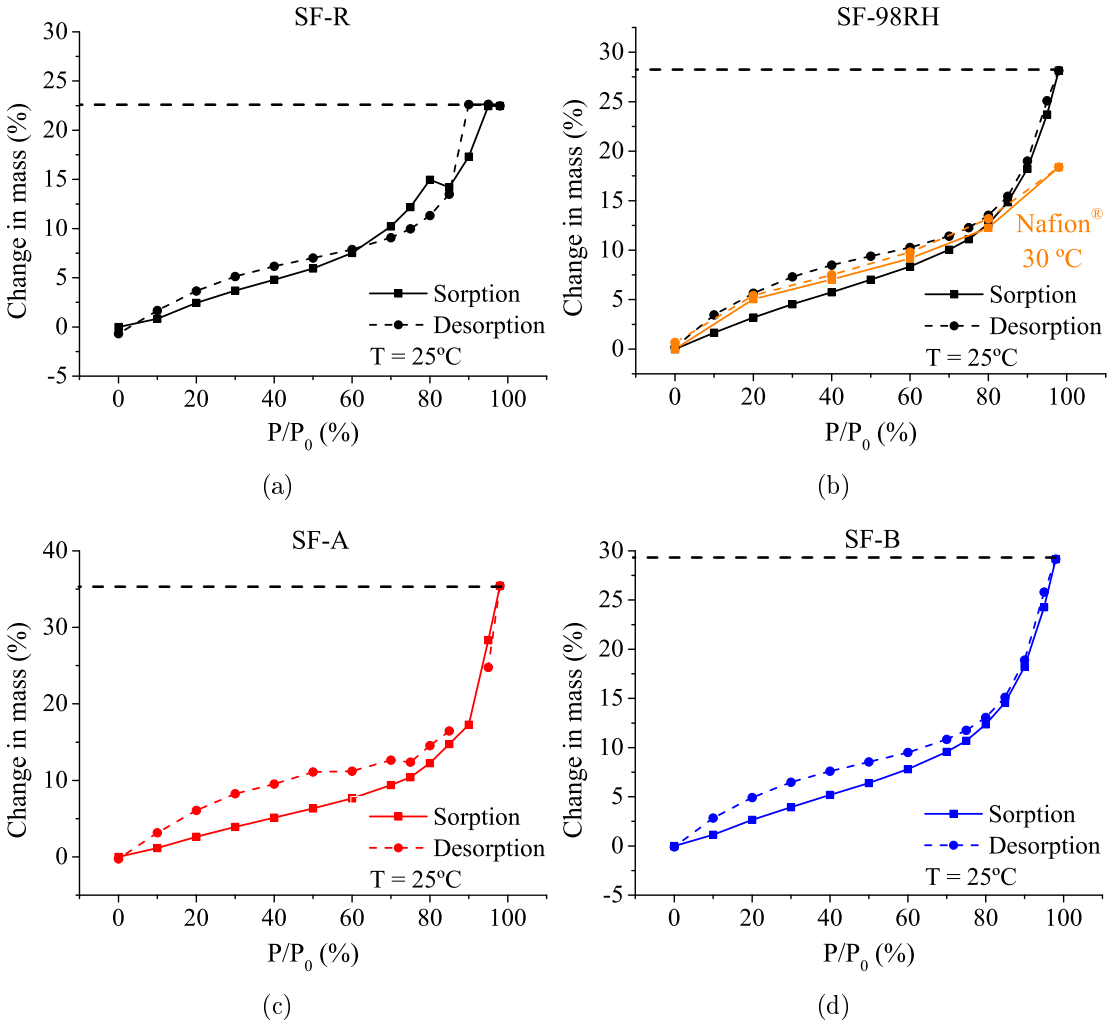

Figure 34 – Sorption isotherm obtained for all the membranes, at 25°C.

It can be seen that the more amorphous membrane (SF-R) presents itself with a slight negative change in mass around 80% RH, which is promptly recovered upon further increase in the water vapor partial pressure. This P/P_0 condition may suggest a structural transition from random coil to the Silk II structure that may occur by the movement of the small hydrophilic blocks inside the micellar structure to the surface and posterior release of water. The occurrence of crystallization in the DVS measurements was after confirmed by XRD, and a clear transition from an amorphous membrane to a similar diffraction pattern of the SF-98RH membrane can be seen in Figure 35.

The results also show that the SF-98RH membrane adsorbs more water, and has a higher value for the maximum change in mass (28%) than the SF-R membrane (23%). This can

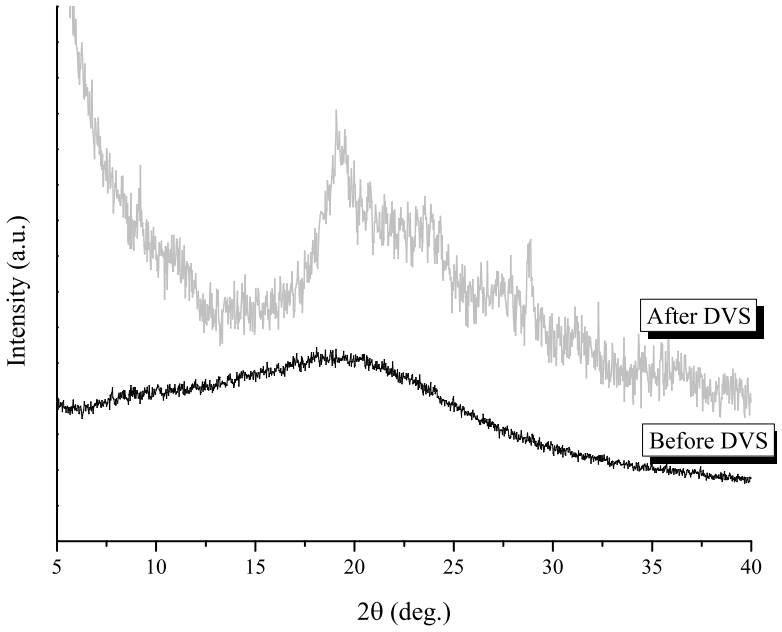

Figure 35 – X-ray diffractogram of the reference membrane (SF-R) before and after DVS measurements. It is possible to observe that the membrane crystallized during the measurements.

be justified by the more organized structure of the SF-98RH membrane formed by the mechanism proposed in Figure 13, where the hydrophilic blocks in the micelles will move to the surface to interact with water, allowing the aggregation of the interior hydrophobic blocks into β-sheets. This structure will therefore withhold a higher content of water at its surface due to its higher surface hydrophilicity. The values obtained are also higher than those presented by Nafion®, which are lower than 20% at 98% RH and 30 °C. [60]

SF-A and SF-B have even higher values for their maximum change in mass of 36% and 29%, respectively, at 25 °C and 98% RH. The higher value for these two membranes is suggested to be due to the disruption caused by degradation with the acid and alkaline treatments on the membrane. The ordered hydrophilic-hydrophobic structure of SF formed by the treatment at 98% RH will be disrupted, and the surface will become disordered, allowing water to enter and exit the structure freely, translating into increased water sorption. The high increase of the change in mass at 90% for the SF-A membrane is probably due to a heterogeneous behavior of the membrane, which might have influencing the measurements performed by the instrument.

Results for the water up-take and swelling ratio studies are presented in Table 3.

The obtained results seem to have a completely inverted tendency in relation to the DVS results. This is once again suggested to be explained by the micellar structure formed by SF. While the SF-R membrane has the highest value for water up-take, the value

Table 3 – Water up-take and swelling ratio results of the SF prepared membranes.

Membrane	Water up-take (%)	Swelling ratio (%)
SF-R	123	17.4
SF-98RH	89,4	12.5
SF-A	60.3	8.30
SF-B	58.3	5.50

lowers for the SF-98RH membrane due to the fact that after crystallization, most of the hydrophilic blocks of the structure will move to the surface of the micelles, thus lowering the capacity for retaining water inside the structure.

After the acid and basic treatments, the occurred hydrolysis inside the membrane will lower the amount of hydrogen bonds available for withholding water inside the structure, and water will easily enter and exit the structure, translating into a lower value of up-take after the membrane is dried with absorbent paper in these studies.

Swelling studies showed that the SF-R membrane shows the highest increase in its thickness. This result is in agreement with the highest value for water-uptake results. The SF-A and SF-B seemed to have lost some capacity for water retention, which also goes in agreement with their water up-take values.

Like the IEC determinations, water up-take and swelling studies were also not repeated to confirm all the obtained results, and therefore there is an associated error to these studies. Water vapor sorption studies are more trustworthy, since they are performed with the assistance of a ultramicrobalance, with a error around 0.1 µg. [60] It is also important to note that the difference between the values obtained in DVS for the maximum change in mass and the values obtained in the water uptake studies is justified by the Schroeder's paradox, which explains that water sorption at saturation level (98% RH) is carried out by a different mechanism than water sorption in liquid water. [71]

4.4. Thermal stability

Since PEFCs work at temperatures up to 220 °C, it is important to evaluate the thermal stability of the prepared SF membranes. Thermogravimetric analysis was performed for all the membranes and the results are compiled in Table 4. The obtained plots are presented in Figure A.6. T_1 is the chosen temperature for comparing water content while T_2 is to compare the degradation of the different membranes.

Table 4 – Main results obtained in TGA for all the SF membranes.

Sample	Δ_{mass} (%)		Residue (%)
	T_1 = 100 °C	T_2 = 260 °C	
SF-R	7	19	21
SF-98RH	5	13	30
SF-A	18	25	26
SF-B	15	21	29

The results suggest that all the SF based membranes undergo degradation around 260 °C, under an inert atmosphere, showing that the membranes are thermally stable until such temperature. The SF-98RH is the most stable membrane, which is probably due to its more crystalline structure.

The SF-R membrane shows a higher mass loss between 25 and 100 °C than the SF-98RH, which suggests it has a higher water content. This goes in accordance with the water up-take results, that suggested higher water retention inside the structure for the SF-R membrane, due to the mechanism of water absorption. SF-98RH could be adsorbing a higher content of water mostly at its surface, making it difficult for water to enter the structure at a higher percentage, while such does not happen to the SF-R membrane.

From all the membranes, SF-A and SF-B membranes lose more weight between 25 °C and 100 °C, suggesting they have a higher water content, in accordance with the DVS results. The weight derivative curves presented in Figures A.6c and A.6d show that both SF-A and SF-B lose water much more faster than the reference and SF-98RH membranes. This tendency goes in accordance with the water-uptake results for these membranes. Since hydrolysis is likely to have disrupted the surface of the micellar structure of SF, the capacity of these membranes to retain water within their structure has lowered, therefore translating into a faster removal of water during TGA. SF-B also shows a faster degradation rate, which might suggest lower thermal stability. Since degradation temperatures for all the membranes are around 260 °C, SF proves to be suitable for working under the temperature range of PEFCs.

4.5. Mechanical properties

In view of the importance of the mechanical properties of polymer electrolytes, the mechanical properties of the prepared membranes were studied by dynamic mechanical analysis and the results are compiled in Figure 36.

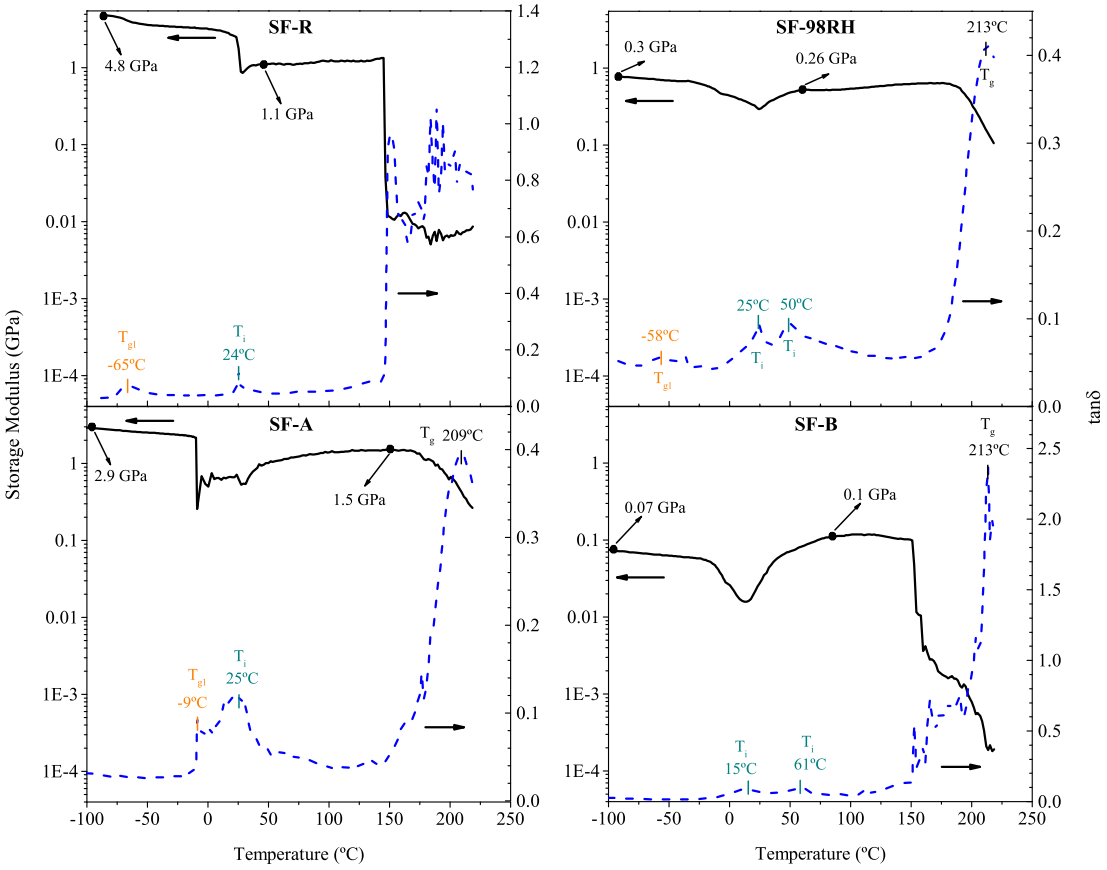

Figure 36 – DMA results of all the prepared membranes. The storage modulus are the black lines while the loss tangent are the blue lines.

Considering that the different water content of these membranes can have an effect on the dimensional stability of the specimen, care should be taken while evaluating their mechanical response. All the membranes have a decrease in storage modulus starting at -20 °C, but only SF-98RH and SF-B seem to recover after that decrease. At 150 °C, SF-R and SF-B have an abrupt drop in storage modulus, associated with membrane degradation whilst for the other two membranes this drop only took place around 220 °C. Considering the loss tangent, other transitions can be observed namely at -58 °C, 25 °C, 50 °C and around 213 °C . The latter is attributed to the glass transition temperature, T_g. Curiously, SF-R does not show a visible T_g. The other transitions observed are associated with different modes of interaction with water.

The other three loss tangent peaks have been attributed to the glass transition temperature, T_{g1} of a more unstable structure made by specific water-peptide interactions, formed by hydrogen bonding between water and peptide (Figure 37a), [44, 45] while the two other peaks (T_i) (Figure 37b) are a suggestion of water

evaporating from the structure, after it became mobile at T_{g1}. [44] At temperatures higher than 50 °C, the structure relaxes and recovers its storage modulus, and has a later glass transition temperature (T_g) at around 213 °C, associated to the breakage of amide-amide linkages (Figure 37c), [44] and then starts degrading.

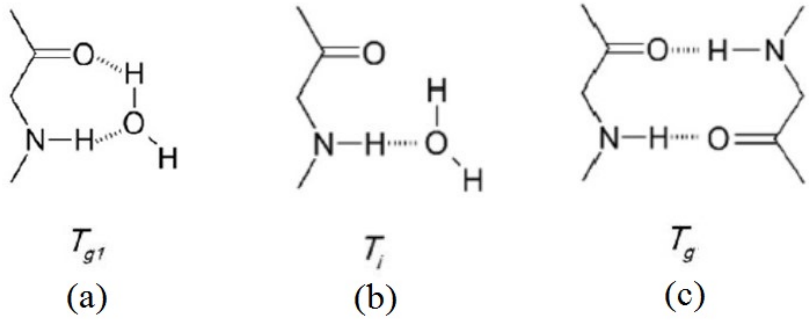

Figure 37 – Interactions assigned to the DMA loss tangent peaks observed. (a) is the water-peptide interaction (b) illustrates the loss of water-peptide interactions which turns water mobile and (c) is the representation of the amide-amide interactions. [45]

In order to confirm that the first three lost tangent peaks were indeed associated with water-peptide interactions, all the membranes were submitted to a second dynamic mechanical analysis, with two separate scans. The first scan was performed from -100 °C to 120 °C, in order to attempt the removal of all the water present inside the structure which was followed by a second scan from -100 °C to 240 °C. The results of the SF-98RH membrane are presented in Figure 38, while the DMA results of the SF-R, SF-A and SF-B are presented in Figures A.7-A.10. The SF-B membrane could not be analyzed in the second scan, due to its fragile behavior, that caused it to break after the first scan.

In the first scan, the peaks associated to T_{g1} and T_i are detected, while in the second scan they disappear almost completely. This suggests that the three loss tangent peaks were indeed associated to water-peptide interactions. This is a consistent results with the other membranes. The obtained values for storage modulus are higher than those presented by Nafion® and SF also shows higher glass transition and degradation temperatures, which prove that SF has improved viscoelastic and thermal properties, again indicating that it can be used in PEFCs working temperatures.

Preliminary tensile tests were also carried out to get an idea of the mechanical properties of the prepared membranes under constant load. The obtained stress-strain curves are presented in Figure 39 while the results are presented in Table 5, showing that the mechanical properties of SF are severely affected by the fiber dissolution and subsequent

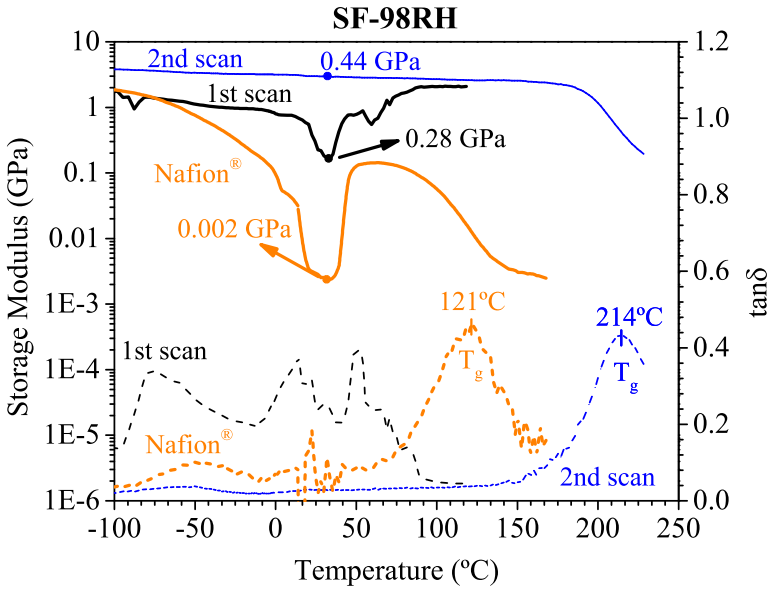

Figure 38 – Second analysis performed on the SF-98RH membrane. The black lines are from the first scan while the blue lines are from the second scan. Storage modulus is in full lines while loss tangent is in dashed lines. DMA for Nafion® is also presented (in orange), for comparison. [57]

casting. For comparison purposes, values for bacterial cellulose and of the SF-fibers are also presented in Table 5.

Table 5 – Tensile testing results.

Sample	Specimen no.	Young's Modulus (MPa)	Tensile Strength (MPa)	Elongation at break (%)
BC [55]	5	15000 ± 470	221 ± 4	2.4 ± 0.2
SF-Fibers [40]	–	10000 - 17000	300-740	4 - 16
SF-R	6	3994 ± 377	52 ± 6	1,6 ± 0.3
SF-98RH	4	1803 ± 169	26 ± 1	1,9 ± 0.2

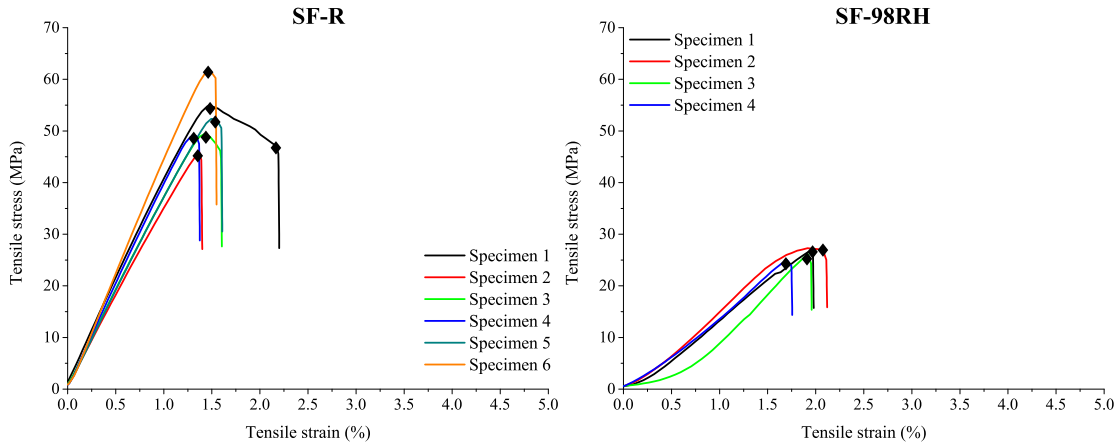

(a) (b)

Figure 39 – Stress-strain curves obtained for the membranes (a) SF-R (b) SF-98RH.

The elastic modulus, tensile strength and elongation at break of the prepared membranes are significantly lower than those of bacterial cellulose. These results are also very much lower than the ones presented by the fibroin fibers, due to both the dissolution with LiBr and the degumming procedure with Na_2CO_3, which is also reported to cause some fibroin degradation. [68]

One can see the elastic modulus of the SF-98RH membrane is lower than that of SF-R despite of the higher crystalline content of the former. In turn, the elongation at break is higher for SF-98RH than that of SF-R. This may be explained by he higher content of water in the post-treated membrane which acts as a plasticizer thus conferring it ductility.

SF-A and SF-B data are not presented as the reduced number of specimen did not allow any kind of truthful comparison with the other membranes.

4.6. Electrical characterization

In order to be able to be used as a possible material for polymer electrolytes, SF's electrical conductivity must of course be investigated. Figure 40 shows the normalized Nyquist plots for the SF-98RH, obtained in the TP measurements, for two limit temperatures.

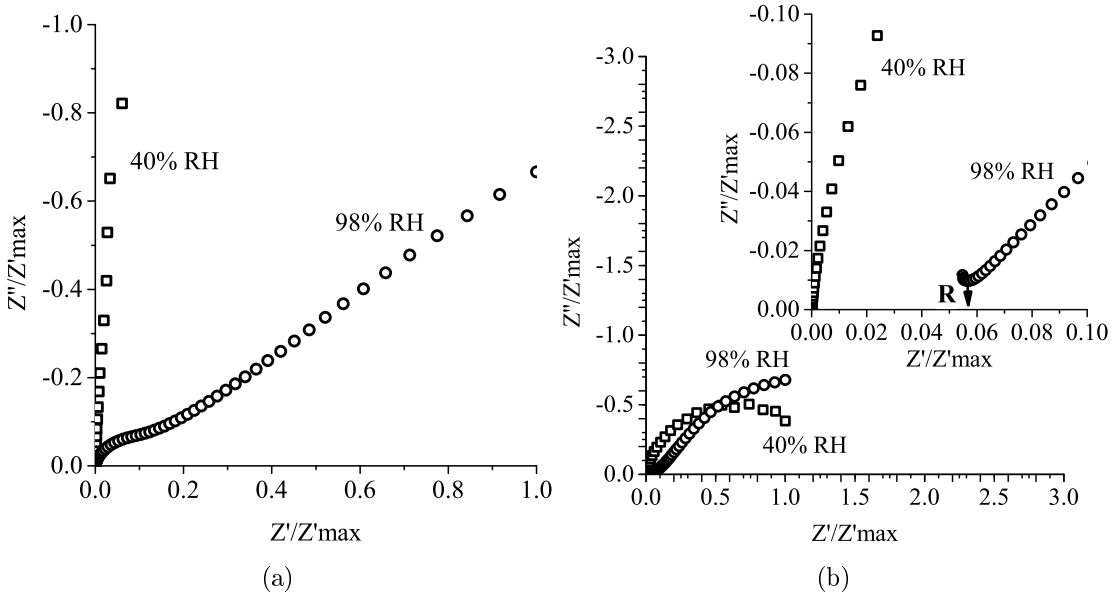

Figure 40 – Normalized impedance spectra obtained for the TP measurements of the SF-98RH membrane, at (a) 30 °C and (b) 94 °C.

At 30 °C and 40% RH, the semi-circle aspect of the spectra starts to be seen, and the ohmic resistance can be taken, by the amplitude of the semi-circle. It can also be seen

that the influence of the electrode starts to be more visible at 98% RH. At 94 °C, the ohmic resistance decreases with the temperature increase, due to the thermal activation of the conductive phenomena.

At 94°C, the increase in RH to 98% causes a decrease of the ohmic resistance and there is a significant increase in the relaxation frequency of the transport process, causing the semi-circle to be no longer visible. The increase in RH also confirms that the increased water content produces higher values for conductivity. In the spectra zoomed in at Figure 40b, the ohmic resistance of the membrane will correspond to the value of Z' pointed out by the arrow. The other membranes have similar spectra, and in some lower temperature and lower RH conditions, the values for resistance are too high to be measured (in excess of 10 MΩ). The influence of the experimental setup also started to be visible at higher temperatures and RH, with an inductive contribution, which was previously corrected in these results. Nyquist plots before and after the correction are shown in Section A.8.

The Arrhenius plots of the in-plane (IP) and through-plane (TP) conductivity of all the membranes are presented in Figure 41. The plots confirm the conclusions drawn from the impedance spectra. The conductivity increases with both the increase in temperature and the increase in RH.

The highest conductivities are the ones demonstrated by the SF-98RH membrane, a result than can be easily correlated with the DVS results. Since SF-98RH adsorbs more water at its surface than the SF-R membrane, because of its more hydrophilic structure on the outer layer of the micellar structure, it will have increased conductivity.

However, the conductivity measurements were performed in humidity steps for each temperature. Because SF is suggested to start crystallizing at 80% RH, the SF-R membrane could have suffered a structural rearrange into a similar structure as SF-98RH at 30 °C, justifying the apparent increase of conductivities at the latest temperatures/humidities for SF-R. In Figure 42, this crystallization was confirmed to happen, by performing XRD after the conductivity measurements. The other membranes however, showed no signs of change in their structure after the measurements.

The SF-A and SF-B membranes have lower conductivity than the other membranes, which again might be correlated with hydrolysis taking place, affecting the structural order of SF, thus negatively affecting transport properties such as conductivity.

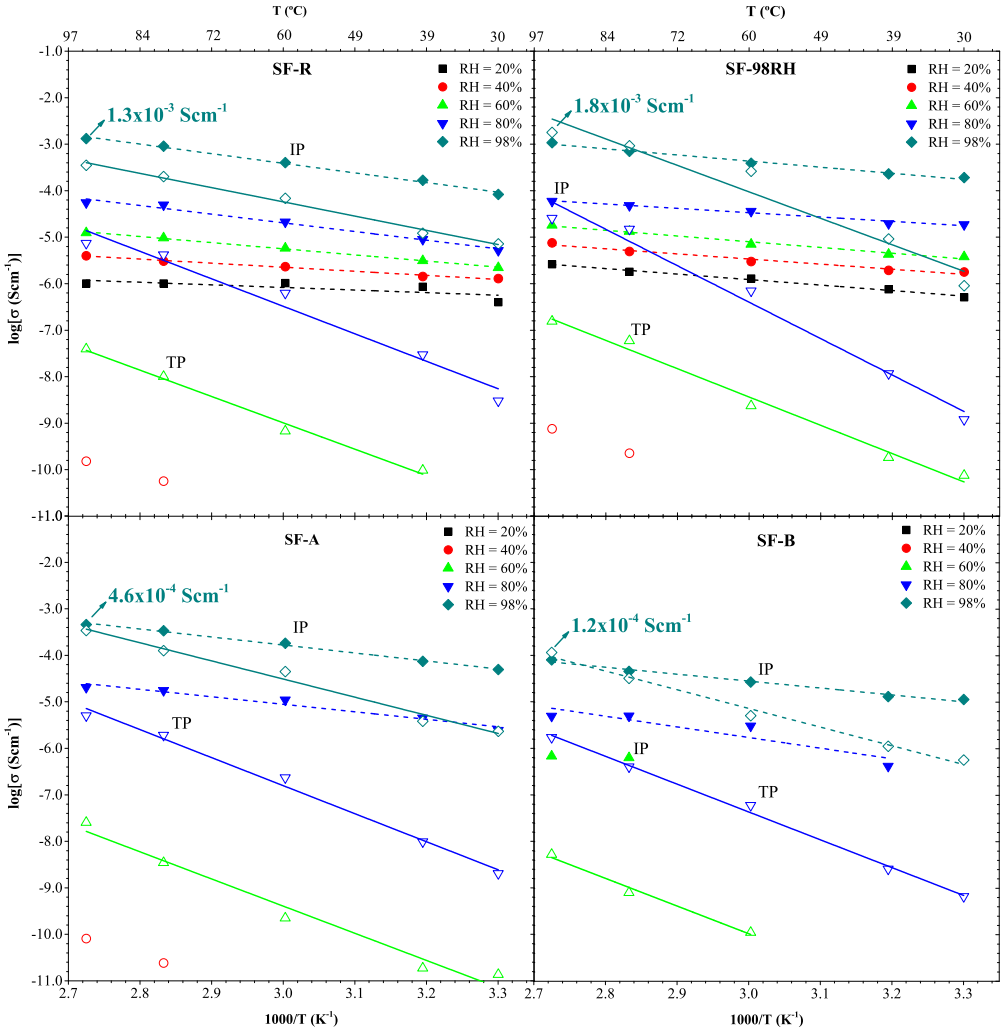

Figure 41 – Arrhenius plots for the conductivity of all the SF-based membranes, measured under variable humidity. The full lines are for the through-plane measurements while the dashed lines are for in-plane measurements.

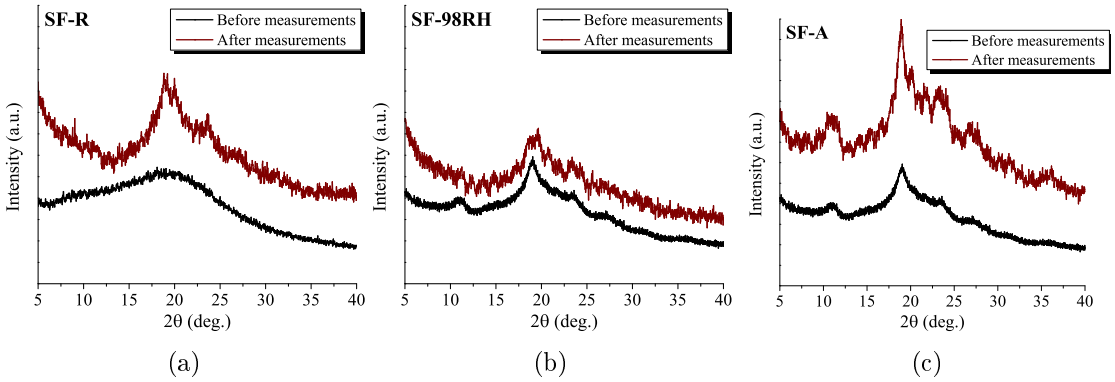

Figure 42 – X-ray diffractograms of the membranes (a) SF-R (b) SF-98RH and (c) SF-A before and after the in-plane conductivity measurements. The SF-B membrane broke and therefore could not be analyzed.

The data points present an Arrhenius-type behavior (linear), and so the apparent activation energies of the transport phenomena can be obtained, using Equation 4.2, after rearranging Equation 4.1.

$$\sigma = \frac{\sigma_0}{T} \times \exp(-E_a/RT) \tag{4.1}$$

$$ln\frac{\sigma \times T}{\sigma_0} = -\frac{E_a}{R} \times \frac{1}{T} \tag{4.2}$$

σ represents the conductivity in S.cm^{-1}, E$_a$ the activation energy in J.mol^{-1} and T the temperature, in K. The obtained apparent activation energies are presented in Table 6.

Table 6 – Apparent activation energies obtained for the IP and TP measurements.

Sample	IP/TP E$_a$ (kJ.mol^{-1})				
	20% RH	40% RH	60% RH	80% RH	98% RH
SF-R	13/–	22/–	28/111	39/116	42/61
SF-98RH	25/–	27/–	20/119	28/153	42/112
SF-A	–/–	–/–	–/130	30/118	35/77
SF-B	–/–	–/–	–/–	47/117	34/80

The high difference between IP and TP results in conductivity is not usual, because, as it was explained in the Materials and Methods chapter, the high surface area S and the relatively low thickness h should result in lower values for ohmic resistance in TP measurements, and not the opposite, as it happens with SF membranes.

This unusual tendency could be somehow explained by structure heterogeneity of the membranes, for example due to the micellar structure formed by self-assembly. If indeed the highest amount of large hydrophilic blocks are on the surface of the structure and the large hydrophobic blocks aggregated inside, transport IP is suggested to be facilitated by the hydrophilic behavior of the membrane's surface, while TP conductivity has lower values for conductivity and higher activation energies due to the hydrophobic behavior of the inside of the structure, which translates into limited diffusion through the membrane. A scheme representing this difference in presented in Figure 43.

If one considers the blue layer as the most hydrophilic/conductive part and they yellow as the most hydrophobic, they will be, respectively, characterized by the equivalent electrical resistances R$_1$ and R$_2$ so that R$_2$ >> R$_1$. Assuming simple associations of these resistances according to a series (TP measurements) or parallel (IP

measurements) model, the equivalent total resistance is given by Equations 4.3 and 4.4, respectively.

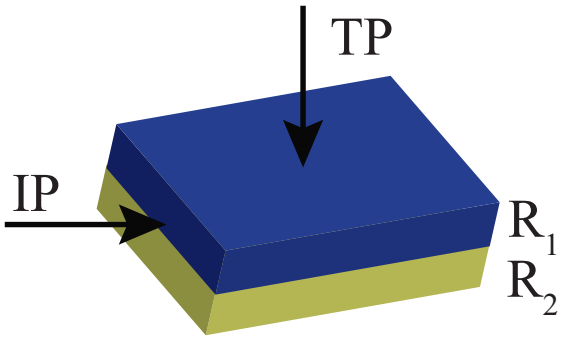

Figure 43 – Suggested scheme for the heterogeneous behavior of SF membranes that produced lower values for TP conductivity.

$$R_{total}\,(IP) = \frac{R_1 \times R_2}{R_1 + R_2} \approx R_1 \tag{4.3}$$

$$R_{total}\,(TP) = R_1 + R_2 \approx R_2 \tag{4.4}$$

In the TP case, the conductivity is largely controlled by the more resistant layer, whereas in the IP configuration, it is the most conductive layer that conducts the process. It can also be seen that, at higher temperatures, the TP results become much more closer to the IP results, and it even looks as if there is a new value for activation energy. This is suggested to be due to the fact that with the temperature increase, the structural rearrange is facilitated in the hydrophobic (yellow) layer and it will therefore become more conductive.

This is a suggested explanation for the unusual tendency of obtaining higher values for conductivity in IP measurements, and the confirmation of such heterogeneous structure stays as a possible task for future work. Although the conductivities have generally lower values than Nafion® and BC, [72] SF still shows promising thermal, mechanical and water sorption properties, and could be a valuable candidate for application as an electrolyte, if functionalized and/or combined with other, more conductive materials.

5. Conclusions and future work

The study performed on SF allowed a comprehensive understanding of the properties of this protein and the influence of water on the structure organization.

After the optimization of the preparation procedures, reproductive SF membranes were produced and their chemical stability evaluated by acid and base treatments. Whilst membrane post-treatment at 98% RH enhanced the formation of β-sheet structures, exposure to acid or base seems to have caused degradation. Gel permeation chromatography results obtained for fibroin solutions treated with acid and with base sustain this hypothesis.

Thermal stability and mechanical properties were also analyzed and showed promising results, with degradation temperatures above PEFCs working conditions. DVS shows high values for water sorption, up to 35% in mass, due to the interestingly ordered structure that SF forms by extensive hydrogen bonding. Water-uptake studies showed good results for water retention as well, both being an asset for working as electrolytes in PEFCs.

Impedance spectroscopy results showed higher values for ionic conductivity for the SF-98RH membrane, probably due to its more organized structure, while SF-A and SF-B had much lower values, as a result of degradation. The results also show great differences between IP and TP configurations. A possible hypothesis for such unusual tendency is thought to be associated to a more heterogeneous structure.

As a follow-up to these conclusions, some suggestions for future work are hereby listed.

- Perform Confocal Raman Microscopy and/or Atomic Force Microscopy to evaluate the SF structure in an attempt to confirm structure heterogeneity and

therefore confirm its correlation with the differences observed between IP and TP conductivity measurements.

- Study the effect of RH and temperature in the membrane post-treatment, namely by Differential Scanning Calorimetry (DSC) and X-ray diffraction.
- Study the use of mixtures of water and polar solvents for the post-treatment atmosphere and evaluate the effect on SF structure, namely by XRD.
- Explore mixing with other materials and/or attempt the functionalization of SF, bearing in mind the risk of compromising the formation of a β-sheet structure.

Bibliography

[1] EG & G Services (Firm) and National Energy Technology Laboratory (U.S.). *Fuel cell handbook [electronic resource] / EG&G Technical Services, Inc.* U.S. Dept. of Energy, Office of Fossil Energy, National Energy Technology Laboratory Morgantown, WV, 7th ed. edition, 2004.

[2] S. Basu. *Recent Trends in Fuel Cell Science and Technology.* Springer New York, 2007.

[3] R.P. O'Hayre. *Fuel cell fundamentals.* John Wiley & Sons, 2006.

[4] Jin Ran, Liang Wu, Yubin He, Zhengjin Yang, Yaoming Wang, Chenxiao Jiang, Liang Ge, Erigene Bakangura, and Tongwen Xu. Ion exchange membranes: New developments and applications. *Journal of Membrane Science*, 522:267 – 291, 2017.

[5] Frank de Bruijn. The current status of fuel cell technology for mobile and stationary applications. *Green Chemistry*, 7:132–150, 2005.

[6] Gordon R Whitnah, Wesley C Borgeson, and Harvey E Henjum. Flugrocarbon vinyl ether polymers. *United States Patent Office*, 1(US3282875), 1964.

[7] M. Rikukawa and K. Sanui. Proton-conducting polymer electrolyte membranes based on hydrocarbon polymers. *Progress in Polymer Science*, 25(10):1463–1502, 2000.

[8] Shimon Ochi, Osamu Kamishima, Junichiro Mizusaki, and Junichi Kawamura. Investigation of proton diffusion in nafion®117 membrane by electrical conductivity and nmr. *State Ionics*, 180(6):580 – 584, 2009.

[9] Pyoungho Choi, Nikhil H. Jalani, and Ravindra Datta. Thermodynamics and proton transport in nafion ii. proton diffusion mechanisms and conductivity. *Journal of The Electrochemical Society*, 152:E123–E130, 03 2005.

[10] Klaus-Dieter Kreuer, Stephen J. Paddison, Eckhard Spohr, and Michael Schuster. Transport in proton conductors for fuel-cell applications: Simulations, elementary reactions, and phenomenology. *Chemical Reviews*, 104(10):4637–4678, Oct 2004.

[11] S.J. Peighambardoust, S. Rowshanzamir, and M. Amjadi. Review of the proton exchange membranes for fuel cell applications. *International Journal of Hydrogen Energy*, 35(17):9349 – 9384, 2010.

[12] Adolfo Iulianelli and Angelo Basile. Sulfonated peek-based polymers in pemfc and dmfc applications: A review. *International Journal of Hydrogen Energy*, 37(20):15241 – 15255, 2012.

[13] B. Smitha, S. Sridhar, and A.A. Khan. Solid polymer electrolyte membranes for fuel cell applications—a review. *Journal of Membrane Science*, 259(1):10 – 26, 2005.

[14] Jia Ma and Yogeshwar Sahai. Chitosan biopolymer for fuel cell applications. *Carbohydrate Polymers*, 92(2):955 – 975, 2013.

[15] Zhongyi Jiang, Xiaohong Zheng, Hong Wu, Jingtao Wang, and Yabo Wang. Proton conducting cs/p(aa-amps) membrane with reduced methanol permeability for dmfcs. *Journal of Power Sources*, 180(1):143 – 153, 2008.

[16] M. F. Shukur, R. Ithnin, and M. F. Z. Kadir. Electrical properties of proton conducting solid biopolymer electrolytes based on starch–chitosan blend. *Ionics*, 20(7):977–999, Jul 2014.

[17] Chung-Mu Yu and Lin-Chi Chen. Turning glucose and starch into electricity with an enzymatic fuel cell. *Engineering in Agriculture, Environment and Food*, 2(1):1 – 6, 2009.

[18] Y.-H. Percival Zhang, Barbara R. Evans, Jonathan R. Mielenz, Robert C. Hopkins, and Michael W.W. Adams. High-yield hydrogen production from starch and water by a synthetic enzymatic pathway. *PLOS ONE*, 2(5):1–6, 05 2007.

[19] Tiago D. O. Gadim, Andrea G. P. R. Figueiredo, Nataly C. Rosero-Navarro, Carla Vilela, José A. F. Gamelas, Ana Barros-Timmons, Carlos Pascoal Neto, Armando J. D. Silvestre, Carmen S. R. Freire, and Filipe M. L. Figueiredo. Nanostructured bacterial cellulose-poly(4-styrene sulfonic acid) composite membranes with high storage modulus and protonic conductivity. *ACS Applied Materials & Interfaces*, 6(10):7864–7875, May 2014.

[20] Faezah Esa, Siti Masrinda Tasirin, and Norliza Abd Rahman. Overview of bacterial cellulose production and application. *Agriculture and Agricultural Science Procedia*, 2:113 – 119, 2014.

[21] Rui F. P. Pereira, Maria M. Silva, and Verónica de Zea Bermudez. Bombyx mori silk fibers: An outstanding family of materials. *Macromolecular Materials and Engineering*, 300(12):1171–1198, 2015.

[22] K. Murugesh Babu. 1 - introduction to silk and sericulture. In K. Murugesh Babu, editor, *Silk*, Woodhead Publishing Series in Textiles, pages 1 – 32. Woodhead Publishing, 2013.

[23] R.M. Kozłowski. *Handbook of Natural Fibres: Processing and Applications*. Woodhead Publishing Series in Textiles. Elsevier Science, 2012.

[24] John G. Hardy, Lin M. Römer, and Thomas R. Scheibel. Polymeric materials based on silk proteins. *Polymer*, 49(20):4309 – 4327, 2008.

[25] C. Spring and J. Hudson. *Silk in Africa*. Fabric Folios. British Museum Press, 2002.

[26] Ting-Ting Cao, Yuan-Jing Wang, and Yu-Qing Zhang. Effect of strongly alkaline electrolyzed water on silk degumming and the physical properties of the fibroin fiber. *PLOS ONE*, 8(6):1–8, 06 2013.

[27] Regina Inês Kunz, Rose Meire Costa Brancalhão, Lucinéia de Fátima Chasko Ribeiro, and Maria Raquel Marçal Natali. Silkworm sericin: Properties and biomedical applications. *BioMed Research International*, 2016:8175701, Nov 2016.

[28] Lallepak Lamboni, Mario Gauthier, Guang Yang, and Qun Wang. Silk sericin: A versatile material for tissue engineering and drug delivery. *Biotechnology Advances*, 33(8):1855 – 1867, 2015.

[29] Murat Ersel, Yigit Uyanikgil, Funda Karbek Akarca, Enver Ozcete, Yusuf Ali Altunci, Fatih Karabey, Turker Cavucoglu, Ayfer Meral, Gurkan Yigitturk, and Emel Oyku Cetin. Effects of Silk Sericin on Incision Wound Healing in a Dorsal Skin Flap Wound Healing Rat Model. *Medical Science Monitor*, 22:1064–1078, 2016.

[30] The UniProt Consortium. Uniprot: the universal protein knowledgebase. *Nucleic Acids Research*, 45(D1):D158–D169, 2017.

[31] Abhilasha Rangi and Lalit Jajpura. The biopolymer sericin: Extraction and applications. *Journal of Textile Science and Engineering*, 5(1), 2015.

[32] Tetsuo Asakura, Keiko Okushita, and Mike P. Williamson. Analysis of the structure of bombyx mori silk fibroin by nmr. *Macromolecules*, 48(8):2345–2357, 2015.

[33] Satoshi Inoue, Kazunori Tanaka, Fumio Arisaka, Sumiko Kimura, Kohei Ohtomo, and Shigeki Mizuno. Silk fibroin of Bombyx mori is secreted, assembling a high molecular mass elementary unit consisting of H-chain, L-chain, and P25, with a 6:6:1 molar ratio. *Journal of Biological Chemistry*, 275(51):40517–40528, 2000.

[34] Cong-Zhao Zhou, Fabrice Confalonieri, Michel Jacquet, Roland Perasso, Zhen-Gang Li, and Joel Janin. Silk fibroin: Structural implications of a remarkable amino acid sequence. *Proteins: Structure, Function, and Bioinformatics*, 44(2):119–122, 2001.

[35] Amanda R. Murphy and David L. Kaplan. Biomedical applications of chemically-modified silk fibroin. *Journal of Materials Chemistry*, 19(36):6443–6450, Jun 2009.

[36] Leng-Duei Koh, Yuan Cheng, Choon-Peng Teng, Yin-Win Khin, Xian-Jun Loh, Si-Yin Tee, Michelle Low, Enyi Ye, Hai-Dong Yu, Yong-Wei Zhang, and Ming-Yong Han. Structures, mechanical properties and applications of silk fibroin materials. *Progress in Polymer Science*, 46:86 – 110, 2015.

[37] J.M. Berg, J.L. Tymoczko, and L. Stryer. *Biochemistry, Fifth Edition.* W.H. Freeman, 2002.

[38] Qiang Lu, Hesun Zhu, Cencen Zhang, Feng Zhang, Bing Zhang, and David L. Kaplan. Silk self-assembly mechanisms and control from thermodynamics to kinetics. *Biomacromolecules*, 13(3):826–832, Mar 2012.

[39] Cheng Guotao, Wang Xin, Tao Sijie, Xia Ju, and Xu Shui. Differences in regenerated silk fibroin prepared with different solvent systems: From structures to conformational changes. *Journal of Applied Polymer Science*, 132(22), 2015.

[40] Gregory H Altman, Frank Diaz, Caroline Jakuba, Tara Calabro, Rebecca L Horan, Jingsong Chen, Helen Lu, John Richmond, and David L Kaplan. Silk-based biomaterials. *Biomaterials*, 24(3):401 – 416, 2003.

[41] Shigeo Nakamura, Jun Magoshi, and Yoshiko Magoshi. Thermal properties of silk proteins in silkworms. *ACS Symposium Series*, 544:211–221, 12 1993.

[42] Motta Antonella, Fambri Luca, and Migliaresi Claudio. Regenerated silk fibroin films: Thermal and dynamic mechanical analysis. *Macromolecular Chemistry and Physics*, 203(10-11):1658–1665, Aug 2002.

[43] Qingqing Yuan, Jinrong Yao, Lei Huang, Xin Chen, and Zhengzhong Shao. Correlation between structural and dynamic mechanical transitions of regenerated silk fibroin. *Polymer*, 51(26):6278 – 6283, 2010.

[44] Juan Guan, David Porter, and Fritz Vollrath. Thermally induced changes in dynamic mechanical properties of native silks. *Biomacromolecules*, 14(3):930–937, Mar 2013.

[45] Juan Guan, Yu Wang, Beth Mortimer, Chris Holland, Zhengzhong Shao, David Porter, and Fritz Vollrath. Glass transitions in native silk fibres studied by dynamic mechanical thermal analysis. *Soft Matter*, 12:5926–5936, 2016.

[46] Tomoya Iwazaki, Ryoujin Obinata, Wataru Sugimoto, and Yoshio Takasu. High oxygen-reduction activity of silk-derived activated carbon. *Electrochemistry Communications*, 11(2):376 – 378, 2009.

[47] Xiaoteng Jia, Caiyun Wang, Vijayaraghavan Ranganathan, Bradley Napier, Changchun Yu, Yunfeng Chao, Maria Forsyth, Fiorenzo G Omenetto, Douglas

R. MacFarlane, and Gordon Wallace. A biodegradable thin-film magnesium primary battery using silk fibroin-ionic liquid polymer electrolyte. *ACS Energy Letters*, 2, 03 2017.

[48] Rui Pereira, F. Sentanin, Agnieszka Pawlicka, Cristina Gonçalves, M. Silva, and Verónica Bermudez. Smart windows prepared from bombyx mori silk. *ChemElectroChem*, 3:1084–1097, May 2016.

[49] Rui F. P. Pereira, Ricardo Brito-Pereira, Renato Gonçalves, Marco P. Silva, Carlos M. Costa, Maria Manuela Silva, Verónica de Zea Bermudez, and Senentxu Lanceros-Méndez. Silk fibroin separators: A step toward lithium-ion batteries with enhanced sustainability. *ACS Applied Materials & Interfaces*, 10(6):5385–5394, Feb 2018.

[50] Danielle N. Rockwood, Rucsanda C. Preda, Tuna Yücel, Xiaoqin Wang, Michael L. Lovett, and David L. Kaplan. Materials fabrication from bombyx mori silk fibroin. *Nature Protocols*, 6(10):10.1038/nprot.2011.379, Sep 2011.

[51] Yifeng Huang, Kevin Bailey, Sai Wang, and Xianshe Feng. Silk fibroin films for potential applications in controlled release. *Reactive and Functional Polymers*, 116:57 – 68, 2017.

[52] Charu Vepari and David L. Kaplan. Silk as a biomaterial. *Progress in Polymer Science*, 32(8-9):991–1007, 2007.

[53] Kenjiro Yazawa, Kana Ishida, Hiroyasu Masunaga, Takaaki Hikima, and Keiji Numata. Influence of water content on the b-sheet formation, thermal stability, water removal, and mechanical properties of silk materials. *Biomacromolecules*, 17(3):1057–1066, Mar 2016.

[54] The Editors of Encycopaedia Britannica. Ion-exchange capacity. URL: https://www.britannica.com/science/ion-exchange-capacity, 2016. Accessed: 2018-05-15.

[55] Carla Vilela, Nuno Sousa, Ricardo J.B. Pinto, Armando J.D. Silvestre, Filipe M.L. Figueiredo, and Carmen S.R. Freire. Exploiting poly(ionic liquids) and nanocellulose for the development of bio-based anion-exchange membranes. *Biomass and Bioenergy*, 100:116 – 125, 2017.

[56] Y. Zhou, G. Lin, A.J. Shih, and S.J. Hu. Assembly pressure and membrane swelling in pem fuel cells. *Journal of Power Sources*, 192(2):544 – 551, 2009.

[57] Nataly C. Rosero-Navarro, Eddy M. Domingues, Nuno Sousa, Paula Ferreira, and Filipe M. Figueiredo. Protonic conductivity and viscoelastic behaviour of nafion® membranes with periodic mesoporous organosilica fillers. *International Journal of Hydrogen Energy*, 39(10):5338 – 5349, 2014.

[58] W. Zhou and Z.L. Wang. *Scanning Microscopy for Nanotechnology: Techniques and Applications*. Springer ebook collection / Chemistry and Materials Science 2005-2008. Springer New York, 2007.

[59] Prime R. Bruce, Bair Harvey E., Vyazovkin Sergey, Gallagher Patrick K., and Riga Alan. *Thermogravimetric Analysis (TGA)*, chapter 3, pages 241–317. Wiley-Blackwell, 2008.

[60] Daniel J. Burnett, Armando R. Garcia, and Frank Thielmann. Measuring moisture sorption and diffusion kinetics on proton exchange membranes using a gravimetric vapor sorption apparatus. *Journal of Power Sources*, 160(1):426 – 430, 2006.

[61] Tal M. Nahir. Impedance spectroscopy: Theory, experiment, and applications, 2nd ed edited by evgenij barsoukov (texas instruments inc.) and j. ross macdonald (university of north carolina, chapel hill). john wiley & sons, inc.: Hoboken, nj.

2005. xvii + 596 pp. $125.00. isbn 0471-64749-7. *Journal of the American Chemical Society*, 127(35):12431–12431, Sep 2005.

[62] M.E. Orazem and B. Tribollet. *Electrochemical Impedance Spectroscopy*. The ECS Series of Texts and Monographs. Wiley, 2011.

[63] Plancha, Maria João Carrilho. Electrólitos poliméricos para sistemas electroquímicos de energia, 2008.

[64] Xiao Hu, Karen Shmelev, Lin Sun, Eun-Seok Gil, Sang-Hyug Park, Peggy Cebe, and David L. Kaplan. Regulation of silk material structure by temperature-controlled water vapor annealing. *Biomacromolecules*, 12(5):1686–1696, May 2011.

[65] Qiang Lu, Xiao Hu, Xiaoqin Wang, Jonathan A. Kluge, Shenzhou Lu, Peggy Cebe, and David L. Kaplan. Water-insoluble silk films with silk i structure. *Acta Biomaterialia*, 6(4):1380 – 1387, 2010.

[66] E. S. Sashina, A. M. Bochek, N. P. Novoselov, and D. A. Kirichenko. Structure and solubility of natural silk fibroin. *Russian Journal of Applied Chemistry*, 79(6):869–876, Jun 2006.

[67] In Chul Um, Hae Yong Kweon, Kwang Gill Lee, and Young Hwan Park. The role of formic acid in solution stability and crystallization of silk protein polymer. *International Journal of Biological Macromolecules*, 33(4):203 – 213, 2003.

[68] Cheng Guotao, Wang Xin, Tao Sijie, Xia Ju, and Xu Shui. Differences in regenerated silk fibroin prepared with different solvent systems: From structures to conformational changes. *Journal of Applied Polymer Science*, 132(22), 2015.

[69] Zhang Shanshan, Li Jiaojiao, Yin Zhuping, Zhang Xiaofeng, Kundu Subhas C., and Lu Shenzhou. Silk fibroin composite membranes for application in corneal regeneration. *Journal of Applied Polymer Science*, 132(32), 2015.

[70] Grínia M. Nogueira, Andrea C.D. Rodas, Carlos A.P. Leite, Carlos Giles, Olga Z. Higa, Bronislaw Polakiewicz, and Marisa M. Beppu. Preparation and characterization of ethanol-treated silk fibroin dense membranes for biomaterials application using waste silk fibers as raw material. *Bioresource Technology*, 101(21):8446 – 8451, 2010.

[71] K.D Kreuer. On the complexity of proton conduction phenomena. *Solid State Ionics*, 136-137:149 – 160, 2000. Proceedings of the 12th International Conference on Solid State Ionics.

[72] Tiago D. O. Gadim. Nafion and nanocellulose: A partnership for greener polymer electrolyte membranes. *Industrial crops and products*, v. 93:pp. 212–218–2016 v.93, 2016.

Appendices

A.1 Abbreviations and names of some of the materials presented in Figure 5

Table A.1 – Abbreviations and names of some of the materials presented in Figure 5 [13].

Abbreviation	Name
NPI	naphthalenic polyimide
BAM3G	ballard advance material of third generation membrane
PBI	polybenzimidazole
PEI	poly(ethyleneimine)
PFCA	perfluorocarboxylic acid
PFSA	perfluorosulfonic acid
PFSI	bis(perfluoroalkylsulfonyl)imide
Poly-AMPS	poly(2-acrylamido-2-methylpropanesulfonic acid)
$PSU(NH_2)_2$	ortho-sulfone aminated polysulfone
PTFE-g-TFS	α,β,β-trifluorostyrene grafted onto poly(tetrafluoroethylene) with post sulfonation
PVDF-g-PSSA	styrene grated on sulfonated poly(vinylidiene fluoride)
P4VP	poly(4-vinyl pyrrolidone)
SPEEK	sulfonated poly(ether ether ketone)
SPPBP	sulfonated poly(4-phenoxy benzoyl-1,4-phenylene)
SPSU	sulfonated polysulfone

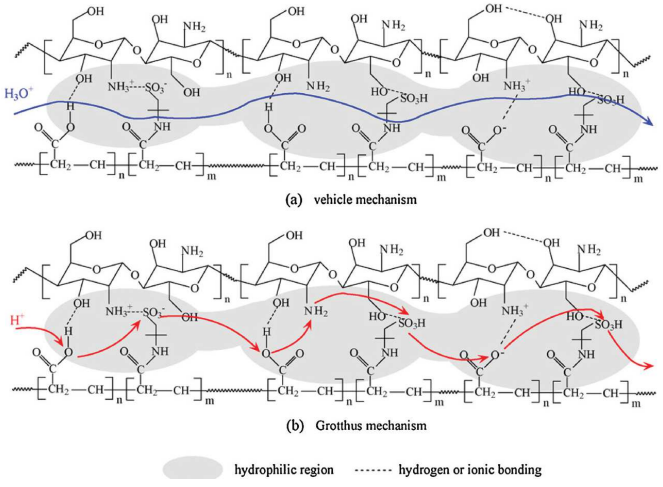

Figure A.1 – Illustration of the proton conduction mechanisms present in chitosan-P(AA-AMPS) blends [14].

A.2 Additional FTIR results

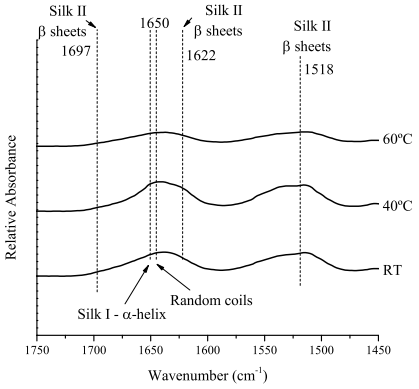

Figure A.2 – FTIR spectra of the membranes prepared under vacuum, at different temperatures. The membranes have signs of an amorphous structure.

A.3 SEM

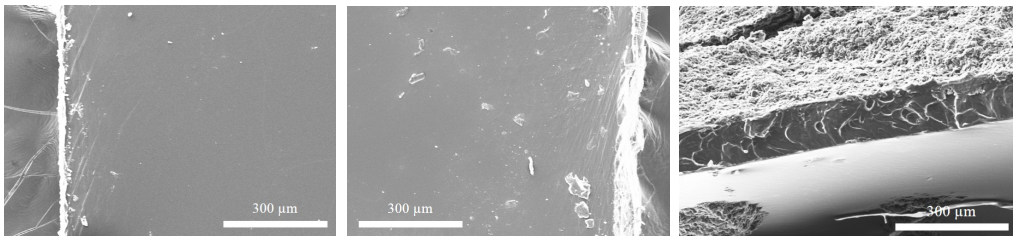

(a) (b) (c)

Figure A.3 – SEM images of the prepared membrane at 40 °C. (a) is the top side of the membrane (b) is the bottom side and (c) is the cross-sectional view.

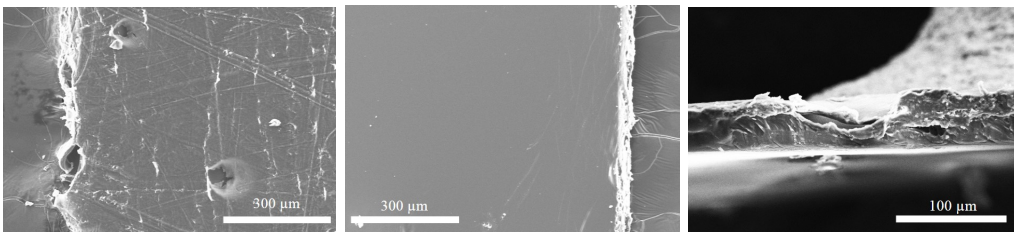

(a) (b) (c)

Figure A.4 – SEM images of the prepared membrane at 60 °C. (a) is the top side of the membrane (b) is the bottom side and (c) is the cross-sectional view.

A.4 GPC

The obtained calibration curve in GPC is presented in Equation A.1.

$$logM_w = 14.82 - 0.6891 \times t_{el} \tag{A.1}$$

Where M_w is the average molecular weight (g.mol^{-1}) and t_{el} is the elution time, in minutes.

A.5 H-fibroin composition

Table A.2 – Amino acid composition of SF's heavy chain [35].

Amino acid	Abbreviation	% (mol/mol)
Alanine	Ala	30.3
Arginine	Arg	0.3
Asparagine	Asn	0.4
Aspartic acid	Asp	0.5
Cysteine	Cys	0.1
Glutamine	Gln	0.6
Glycine	Gly	45.9
Histidine	His	0.1
Isoleucine	Ile	0.2
Leucine	Leu	0.1
Lysine	Lys	0.2
Methionine	Met	0.1
Phenylalanine	Phe	0.6
Proline	Pro	0.3
Serine	Ser	12.1
Threonine	Thr	0.9
Tryptophan	Trp	0.2
Tyrosine	Tyr	5.3
Valine	Val	1.8

A.6 IEC titration curves

In order to determine the ion-exchange capacity, the titration curves of SF-98RH, SF-A and SF-B were analyzed in order to obtain the equivalence point. These titration curves are presented in Figure A.5.

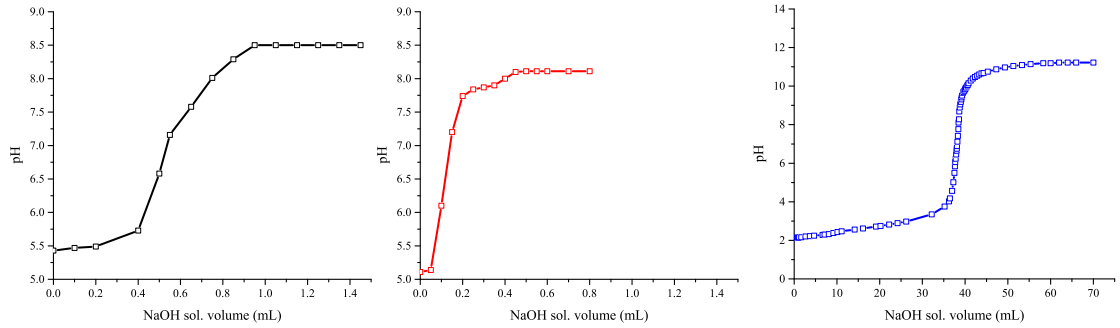

Figure A.5 – Titration curves obtained in the IEC studies for the membranes (a) SF-98RH (b) SF-A and (c) SF-B.

A.7 Additional TGA and DMA data

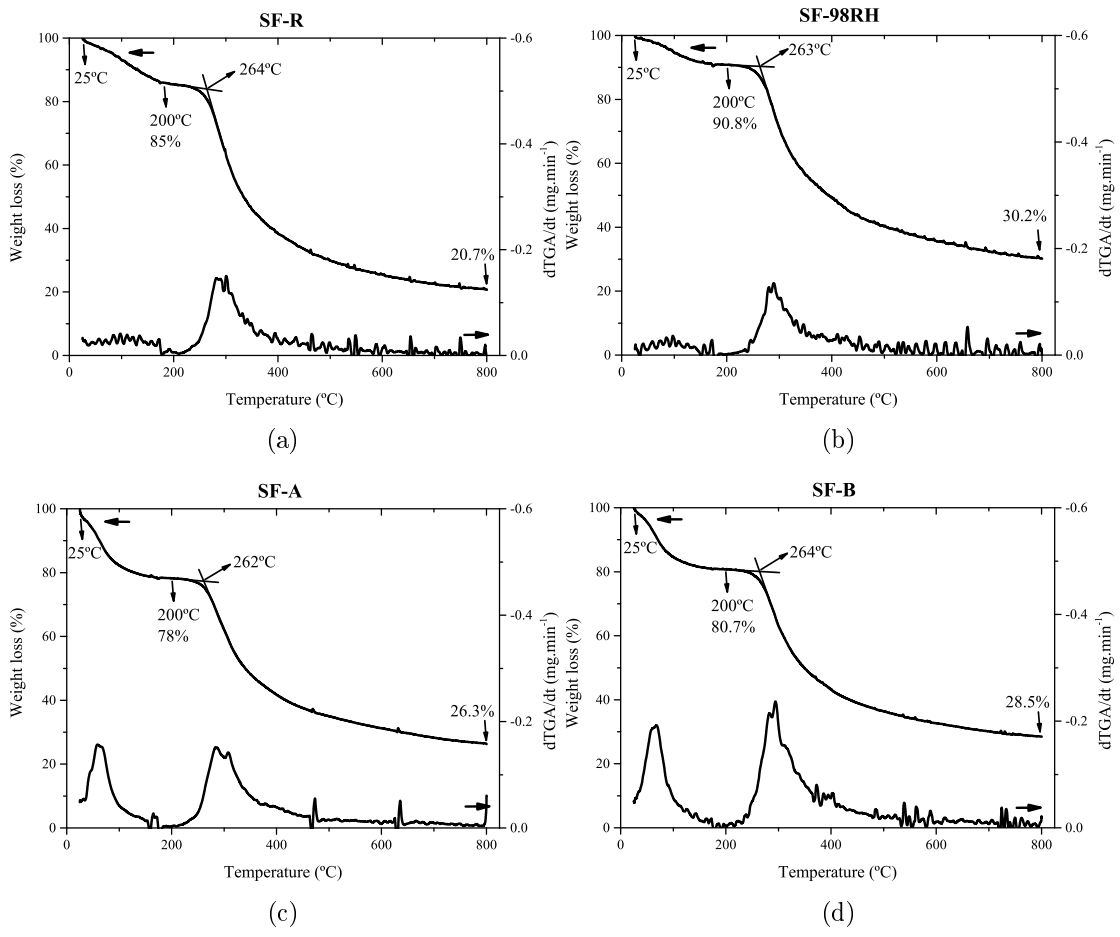

Figure A.6 – TGA results obtained for all the prepared membranes. (a) is for the reference membrane (b) is for the SF-98RH membrane (c) SF-A and (d) SF-B.

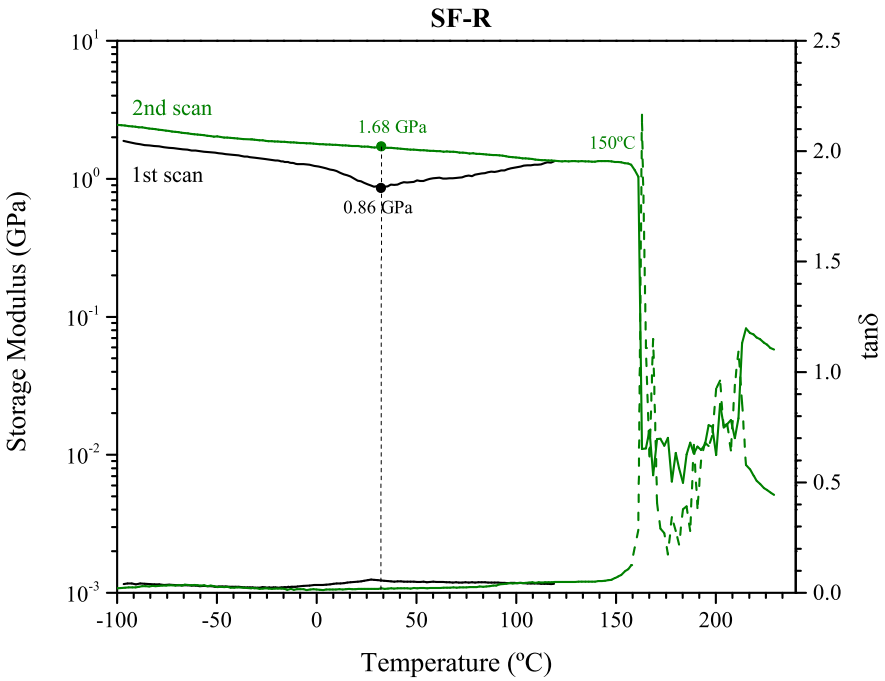

Figure A.7 – Second analysis performed on the SF-R membrane. The black lines are from the first scan while the olive lines are from the second scan. Storage modulus is in full lines while loss tangent is in dashed lines.

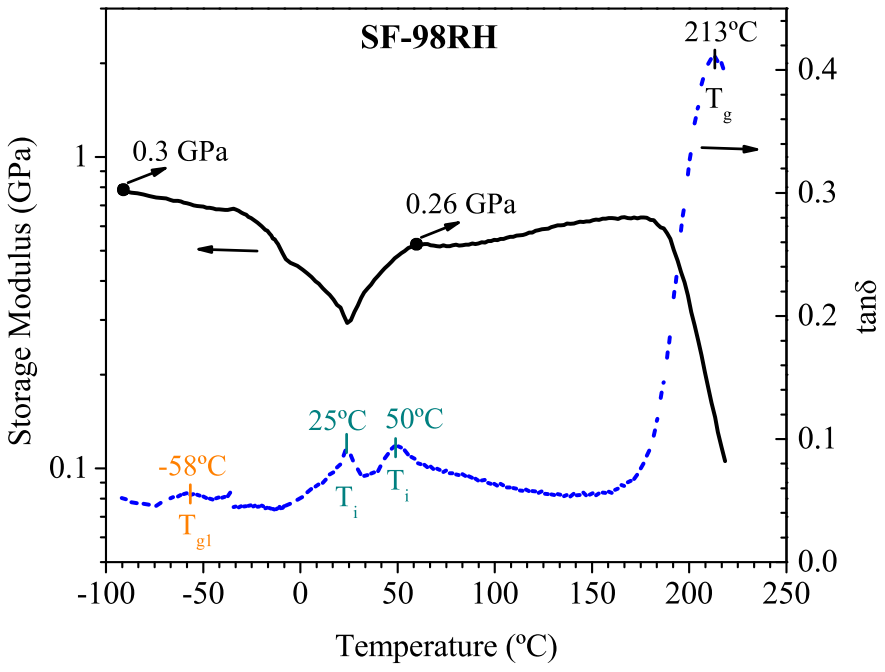

Figure A.8 – First analysis performed on the SF-98RH membrane.

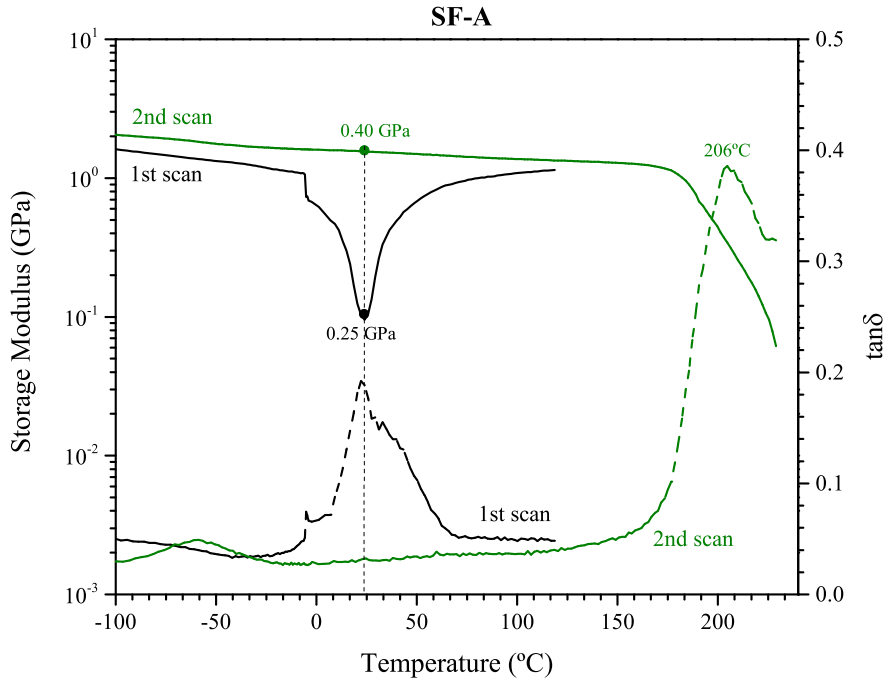

Figure A.9 – Second analysis performed on the SF-A membrane. The black lines are from the first scan while the olive lines are from the second scan. Storage modulus is in full lines while loss tangent is in dashed lines.

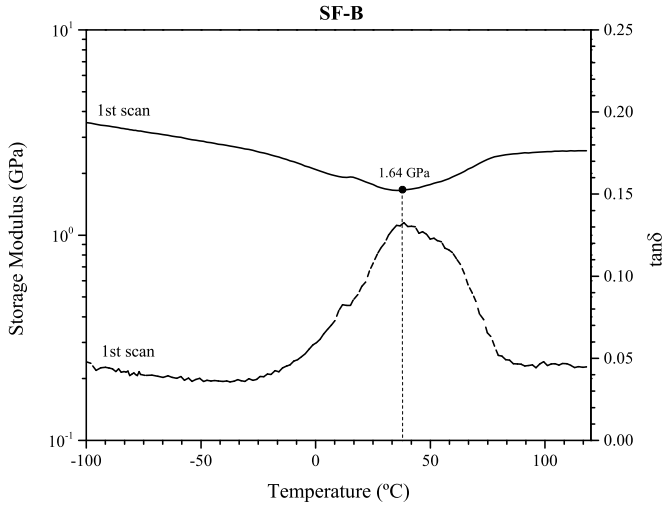

Figure A.10 – Second analysis performed on the SF-B membrane. The black lines are from the first scan. Storage modulus is in full lines while loss tangent is in dashed lines. Since the membrane broke after the first scan, the second scan could not be done (although repeated for another different sample).

A.8 Additional Impedance data

The influence of the experimental setup is mainly attributed to a switch unit installed in the LCR meter, that allows the conductivity measurement of three samples per run.

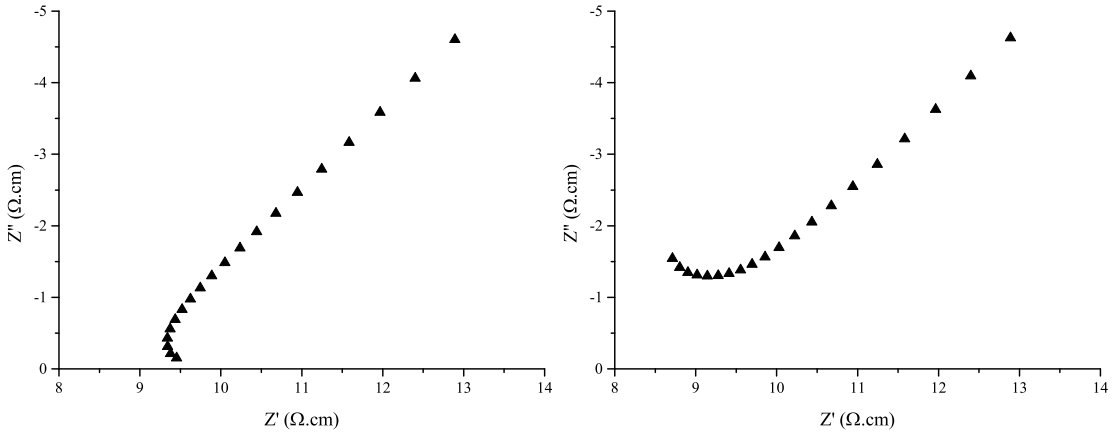

Figure A.11 – Nyquist plots obtained for the TP measurements of the SF-98RH membrane at 94°C and 98% RH (a) before and (b) after the correction.